







Determining the Pyroxene Mineralogies of Vestoids

T. H. Burbine^{1,2} , P. C. Buchanan³ , M. J. Jercinovic⁴ , and R. C. Greenwood⁵ ¹Department of Astronomy, Mount Holyoke College, 50 College Street, South Hadley, MA 01075, USA; tburbine@mholyoke.edu²Planetary Science Institute, 1700 East Fort Lowell, Suite 106, Tucson, AZ 85719, USA³Department of Geology, Kilgore College, Kilgore, TX 75662, USA⁴Department of Geosciences, University of Massachusetts, Amherst, MA 01003, USA⁵The Open University, Walton Hall, Milton Keynes MK7 6AA, UK

Received 2022 April 20; revised 2023 February 5; accepted 2023 February 24; published 2023 May 26

Abstract

Bulk pyroxene compositions were calculated for a number of V-type asteroid spectra using formulae derived by Burbine et al. These formulae were derived by analyzing HED (howardite, eucrite, and diogenite) meteorites and calculate bulk Fs (mol%) and Wo (mol%) contents using derived band centers. Using HEDs with known bulk pyroxene compositions, the uncertainty in the predicted Fs contents was determined to be ± 3 mol%, and the uncertainty in the predicted Wo contents was ± 2 mol%. V-type asteroids tend to have interpreted pyroxene mineralogies consistent primarily with eucrites and howardites. We investigate why diogenitic mineralogies appear so rare among ~ 5 – 10 km V-type asteroids but are much more commonly present among HED meteorites. One possibility is that diogenitic intrusions are extremely “thin” but widespread in Vesta’s eucritic crust. In this scenario, Vestoids (V-type asteroids thought to be derived from Vesta) would be expected to be solid fragments of Vesta. Another possibility is that Vesta’s upper crust has been significantly shattered and diogenitic material would be much less common than the eucritic material in the crust. Vestoids would then be expected to be rubble piles. The belief that most asteroid families were shattered at least twice would argue that Vesta’s crust is also shattered and that Vestoids are rubble piles.

Unified Astronomy Thesaurus concepts: [Meteorites \(1038\)](#); [Asteroids \(72\)](#); [Vesta \(2183\)](#); [Main belt asteroids \(2036\)](#)

Supporting material: machine-readable table

1. Introduction

Asteroid (4) Vesta is one of the most studied objects in the solar system. This scientific interest is primarily due to Vesta’s high brightness compared to most other small bodies, its postulated relationship to specific meteorite groups, and recent spacecraft observations. Vesta is one of the largest asteroids and has long been known to have similar absorption features (Figure 1) to the HED (howardite, eucrite, diogenite) meteorites (e.g., McCord et al. 1970; Larson & Fink 1975; Hiroi et al. 1994). Vesta was one of the targets of NASA’s Dawn mission (Russell et al. 2012; see Figure 2), which spectrally and chemically mapped its surface (e.g., McSween et al. 2013b). Numerous bodies (typically called Vestoids) in the Vesta family and throughout the inner asteroid belt also have reflectance spectra (Figure 1) similar to HEDs (e.g., Binzel & Xu 1993; Duffard et al. 2004; Hardersen et al. 2014, 2015, 2018; DeMeo et al. 2009; Moskovitz et al. 2010; Migliorini et al. 2017); together Vesta and the Vestoids have been classified as V-type asteroids (e.g., Xu et al. 1995; DeMeo et al. 2009). The advent of a medium-resolution 0.7 – 5.3 μm spectrograph (SpeX) at the NASA Infrared Telescope Facility (IRTF; Rayner et al. 2003) has resulted in a large number of high wavelength resolution near-infrared spectral observations of V-type bodies.

Vestoids are evidence that fragments of Vesta can be ejected from Vesta and reach a meteorite-supplying resonance. The

large Rheasilvia basin located at Vesta’s south pole (Figure 3), which formed as a result of an impact, has long been thought to be the source of these Vestoids (e.g., Thomas et al. 1997; Sykes & Vilas 2001). The estimated age of the basin is ~ 0.8 – 0.9 Ga ago (Schenk et al. 2022), which is consistent with the estimated age of the Vesta family (e.g., Asphaug 1997). Even though Vesta is thought to be the predominant source of Vestoids (e.g., Moskovitz et al. 2008a), V-type asteroids have also been identified far from Vesta in the middle and outer part of the asteroid belt (e.g., Lazzaro et al. 2000; Migliorini et al. 2021).

Relationships between Vesta, Vestoids, and HEDs are a case where the meteoritic evidence and asteroidal evidence seem to match extremely well. Dawn observations find olivine to be relatively “rare” on Vesta’s surface (e.g., Ammannito et al. 2013b), and olivine achondrites are also relatively “rare” (e.g., Vaci et al. 2021). Hydrogen, attributed to hydrated silicates, has been identified by Dawn on the surface of Vesta (Prettyman et al. 2012), and carbonaceous chondritic clasts, which contain hydrated silicates, have been identified in HEDs (Zolensky et al. 1996; Buchanan & Mittlefehldt 2003). HEDs with oxygen isotopic compositions different from “typical” HEDs exist (Scott et al. 2009), and V-type asteroids that appear dynamically difficult to derive from Vesta have been identified in the outer asteroid belt (e.g., Lazzaro et al. 2000; Migliorini et al. 2021). Available evidence points to Vesta being the dominant source of HEDs, but a number of other large basaltic bodies appeared to have been present in the asteroid belt (e.g., Burbine et al. 2023).

To determine from Earth the surface mineralogy of Vesta or a Vestoid, reflectance spectra must be collected and analyzed. The visible and near-infrared reflectance spectra of Vesta and



Original content from this work may be used under the terms of the [Creative Commons Attribution 4.0 licence](#). Any further distribution of this work must maintain attribution to the author(s) and the title of the work, journal citation and DOI.

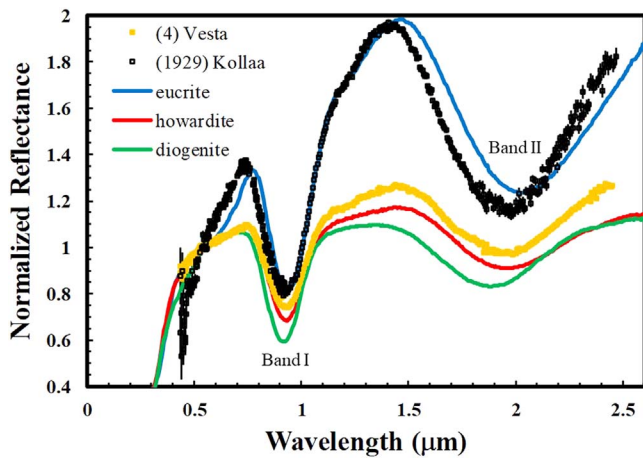


Figure 1. Normalized reflectance spectra of (4) Vesta (orange filled squares), (1929) Kollaa (black open squares), the monomict eucrite Bouvante (blue line), howardite EET 87503 (red line), and diogenite Johnstown (green line). The visible spectra for Vesta and Kollaa are from Bus & Binzel (2002). The IRTF spectrum of Vesta is from Reddy & Sanchez (2016), and the IRTF spectrum of Kollaa is from Bus (2011). The visible spectrum and the near-infrared spectrum are spliced together for each asteroid. The Bouvante spectrum is from Burbine et al. (2001), the EET 87503 spectrum is from Hiroi et al. (1994), and the Johnstown spectrum is from Hiroi et al. (1995). All of the meteorite reflectance spectra were acquired at RELAB. All of the spectra were normalized to unity at $0.55 \mu\text{m}$. The particle sizes of the meteorites are less than $25 \mu\text{m}$. The uncertainties for the asteroid reflectance spectra are 1σ . The uncertainties for the meteorite reflectance spectra are not plotted since they are extremely small. Band I is at $\sim 0.9 \mu\text{m}$, and Band II is at $\sim 1.9 \mu\text{m}$.

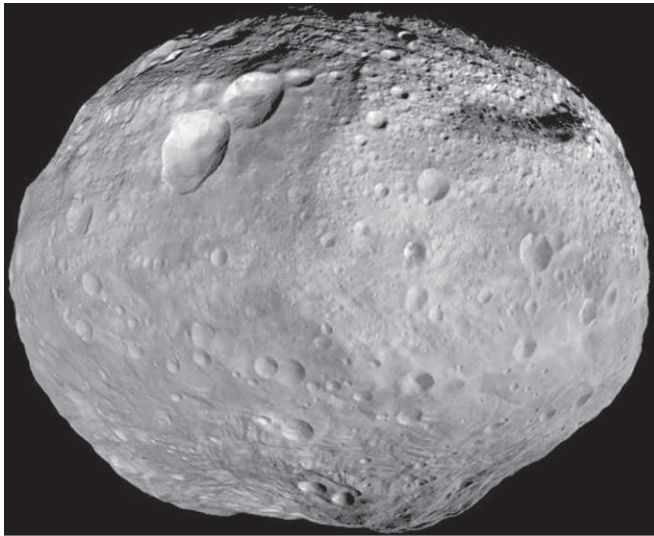


Figure 2. Dawn image of Vesta. Vesta's south pole is at the bottom of the image. Image credit: NASA/JPL-Caltech/UCAL/MPS/DLR/IDA.

Vestoids have absorption features consistent with pyroxene-rich surfaces. The interpreted mineralogies of these bodies are consistent with HEDs, which are predominantly composed of varying proportions of the minerals pyroxene and plagioclase feldspar (e.g., McSween et al. 2012). The advent of a medium-resolution $0.7\text{--}5.3 \mu\text{m}$ spectrograph (SpeX) at the NASA IRTF (Rayner et al. 2003) has resulted in a large number of high wavelength resolution near-infrared spectral observations of Vestoids.

HED spectra are dominated by pyroxene absorption features (e.g., Gaffey 1976; Burns 1993; Beck et al. 2011; Carli et al. 2022). Pyroxenes are single-chain mafic silicates, whose

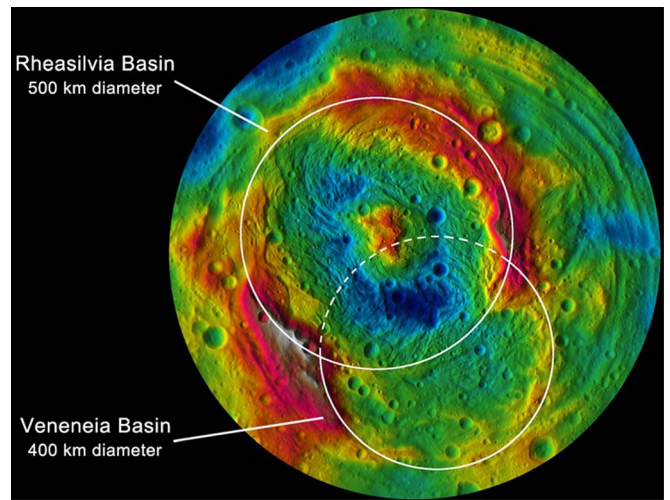


Figure 3. False-color topographic map of Vesta's south pole taken by the Dawn spacecraft. The red color is used for the higher elevations, and the blue color is used for the lower elevations. The younger Rheasilvia basin overlays the older Veneneia basin. Image credit: NASA/JPL-Caltech/UCLA/MPS/DLR/IDA/PSI.

cations are typically Mg, Fe, and Ca. The magnesium-rich endmember of this series is enstatite (En), the iron-rich endmember is ferrosilite (Fs), and the calcium-rich endmember is wollastonite (Wo). Pyroxenes (and, by extension, the bulk compositions of HED meteorites as well) are commonly characterized by a Mg number (Mg#), which is the ratio of the molar Mg content to the sum of molar Mg and Fe contents.

The over 2700 currently identified HEDs can be broken down into a number of different compositional types and subtypes. Diogenites are predominantly composed of magnesian orthopyroxene (e.g., Mittlefehldt et al. 1998). Although a variety of petrogenetic processes have been proposed, these orthopyroxenites are generally thought to be cumulates from Vestan melts (e.g., Grove & Bartels 1992; Fowler et al. 1994; Barrat et al. 2010; Yamaguchi et al. 2011; Greenwood et al. 2014), although the exact details vary. Diogenites are primarily brecciated, but a few unbrecciated examples (e.g., Tatahouine; Barrat et al. 1999) do exist. Although there is a relatively limited compositional range among diogenites, several different petrogenetic groups have been suggested (Hewins 1980; Barrat et al. 2010). Minor components in diogenites commonly include olivine and chromite (e.g., Berkley & Boynton 1992). Diogenites with elevated olivine contents are called olivine diogenites (e.g., Shearer et al. 2010). Polymict diogenites are breccias and contain a relatively small proportion ($<10 \text{ mol}\%$) of eucritic fragments (Delaney et al. 1983; Mittlefehldt et al. 2013).

Eucrites are basalts and gabbros that are primarily composed of pyroxene and anorthite-rich plagioclase with minor amounts of olivine, spinel, and silica. Eucrites have been separated into a number of compositional subtypes (e.g., Papike 1980; Basaltic Volcanism Study Project 1981; Takeda 1997; Mittlefehldt et al. 1998). Compositions of some of the most magnesian eucrites indicate that they are cumulates formed by fractional crystallization of pyroxene and plagioclase from a primitive melt (e.g., Moore County; Treiman 1997) and are, therefore, called cumulate eucrites. The Main Group eucrites (e.g., Juvinas, Sioux County) have been interpreted as partial melts of a primitive mantle material (Stolper 1977). To explain their enrichment in incompatible elements, the Stannern trend

euclrites have been proposed to be due to the contamination of main group eucritic magmas by partial melts of wall rocks (Barrat et al. 2007). The Nuevo Laredo trend euclrites, in contrast, are more Fe-rich and may represent residual melts formed by fractional crystallization of pyroxene and plagioclase from Main Group melts (Warren & Jerde 1987). Righter & Drake (1997) have proposed that Main Group, Stannern trend, and Nuevo Laredo trend euclrites formed as a result of a magma ocean.

Another group of euclrites, called polymict euclrites, are breccias that contain fragments of materials derived from a variety of eucritic sources (Delaney et al. 1984). These polymict euclrites, in some cases, may contain small proportions (<10 mol%) of diogenitic fragments. Monomict euclrites are breccias of only one type of euclrite. Euclrites enriched in Mg include Mg-rich euclrites, cumulate euclrites (e.g., Moama, Moore County), and crystallized impact melts of polymict euclrite or howardite surface areas plus possible crystallized melts derived from anomalously magnesian source regions on Vesta (Mittlefehldt & Lindstrom 1997).

In contrast to the magnesian orthopyroxenes contained in diogenites, the pyroxenes in euclrites are primarily more iron-rich, low-Ca pyroxenes (e.g., pigeonite) with exsolved lamellae of augite. Many of the euclrites are breccias with occasional rock fragments included in a groundmass of mineral grains. There are a few unbrecciated euclrites (Mayne et al. 2009). One unbrecciated euclrite, Ibitira, is known to be chemically (Mittlefehldt 2005) and isotopically (Wiechert et al. 2004; Scott et al. 2009) distinct from other basaltic (noncumulate) euclrites and is believed to have originated on another HED parent body. The best terrestrial analog to these unbrecciated euclrites and the larger basaltic rock fragments in the brecciated HED meteorites are terrestrial basalts.

The third type of HED, the howardites, are polymict breccias that contain mineral and lithic fragments of both eucritic and diogenitic materials (e.g., Mittlefehldt et al. 1998). Howardites have been “arbitrarily” defined as having 10–90 mol% diogenitic materials with complementary proportions of eucritic materials (Delaney et al. 1983) and form a composition and textural continuum with polymict euclrites (Delaney et al. 1984). Some howardites contain fragments of primitive materials, mostly CM chondrites (Zolensky et al. 1996; Buchanan & Mittlefehldt 2003). Howardites provide the best evidence, along with oxygen isotopes (e.g., Greenwood et al. 2014), that most euclrites and diogenites are from the same parent body. Together, all of these HED breccias seem to represent different parts of the regolith of a differentiated asteroid. However, a few euclrite-like meteorites have been found to have oxygen isotopic values that differ from “typical” HEDs and apparently are from other parent bodies than Vesta (Yamaguchi et al. 2002; Scott et al. 2009).

A number of different techniques have been used to determine the mineralogies of Vesta and the Vestoids from their reflectance spectra and to compare them with the mineralogies of the HED meteorites. One method (Gaffey et al. 2002; Burbine et al. 2007, 2009, 2018) uses the positions of the centers of the pyroxene absorption bands, which are functions of the composition of the pyroxenes. The two prominent absorption bands of the Vestoids are the product of the absorptions of a wide variety of pyroxenes that can vary significantly in composition but result in two strong absorptions (typically called Band I and Band II). HEDs have very

distinctive absorption bands compared to other meteorites (e.g., Gaffey 1976). The pyroxenes in euclrites tend to be more Fe- and Ca-rich than the pyroxenes in diogenites, which results in the Band I and Band II centers being at longer wavelengths for eucritic spectra compared to diogenitic spectra (Figure 1). Howardites and cumulate euclrites tend to have band positions intermediate between noncumulate euclrites and diogenites.

Burbine et al. (2018) revised their previously developed formulae (Burbine et al. 2007, 2009) for determining Vestoid bulk pyroxene mineralogies from band center positions derived from their visible and near-infrared reflectance spectra. The Burbine et al. (2018) formulae were used to estimate the bulk pyroxene mineralogies of a number of near-Earth asteroids that were classified as V-type asteroids. The formulae were derived from 13 HED spectra with well-measured bulk pyroxene compositions and calculated the average bulk Fs and Wo contents of the HEDs from their respective Band I and Band II centers. The formulae are

$$Fs(\text{mol}\%) = 1119.4 \times \text{Band I Center}(\mu\text{m}) - 1004.1, \quad (1)$$

$$Wo(\text{mol}\%) = 436.31 \times \text{Band I Center}(\mu\text{m}) - 398.33, \quad (2)$$

$$Fs(\text{mol}\%) = 223.15 \times \text{Band II Center}(\mu\text{m}) - 398.91, \quad (3)$$

and

$$Wo(\text{mol}\%) = 85.342 \times \text{Band II Center}(\mu\text{m}) - 159.21. \quad (4)$$

A number of previous studies (e.g., Mayne et al. 2011; Hardersen et al. 2014, 2015, 2018; Moskovitz et al. 2010) have analyzed Vestoid near-infrared reflectance spectra. We have compiled publicly available main-belt and Mars-crossing V-type spectra from these different studies and analyzed them using the Burbine et al. (2018) equations for determining bulk pyroxene mineralogies. Our hope is that by studying a relatively large number of objects (71 spectra of 49 objects) and using meteorites as a guide, we can gain insight on the compositional structure of Vesta and the relationship between Vesta and the Vestoids. We will first test the Burbine et al. (2018) formulae to see how well these equations determine the bulk pyroxene mineralogies of some newly measured HED reflectance spectra. We will then see how well we can determine the bulk pyroxene mineralogies for a large number of HEDs based on their spectra. We will then determine bulk pyroxene mineralogies of a number of V-type spectra to determine the best meteoritic analogs for each object. Finally, we will look at compositional trends among the Vestoids to try to understand the compositional structure of Vesta.

2. Testing the Formulae Using Meteorite Spectra

2.1. Newly Measured HEDs

To explicitly test how well these formulae determine bulk pyroxene mineralogies of HEDs, we requested from the Meteorite Working Group three relatively small (~50 mg) Antarctic HED chips for spectral measurements. We also requested thin sections for electron microprobe (EPMA) analysis. The meteorites were polymict euclrite ALHA76005, howardite GRO 95574, and diogenite LAP 03630. Each meteorite had a weathering grade of A.

Each chip was powdered to grain size fractions of 25–125 μm . These powders were sent to RELAB for the measurement of bidirectional spectral reflectance. Bidirectional spectral reflectance is the ratio of the reflected radiant flux from

Table 1
Band Centers and 1σ Uncertainties for Newly Measured Meteorites HEDs

Meteorite	Type	RELAB ID	Band I Center	Band II Center
LAP 03630	diogenite	TB-THB-157	0.922 ± 0.004	1.880 ± 0.000
GRO 95574	howardite	TB-THB-156	0.935 ± 0.002	1.951 ± 0.002
ALHA76005	eucrite-pmict	TB-THB-155	0.940 ± 0.001	1.990 ± 0.000

Note. The type of meteorite and its RELAB ID for each spectrum are also listed. We use the abbreviation *eucrite-pmict* for a polymict eucrite.

an object to a “perfect” reflector under a similar geometry and the same single-direction illumination. The incident angle was 30° , and the emission angle was 0° . The wavelength range was 0.300 to $2.550 \mu\text{m}$ with $0.005 \mu\text{m}$ increments.

The reflectance spectra of the three meteorites are displayed in Figure 4. We note that the LAP 03630 spectrum, which was measured from a relatively small sample, had a number of slight absorption features in the visible and at $\sim 2.3 \mu\text{m}$. These features may be due to terrestrial weathering and/or contamination from plastic from the vial. However, these features do not appear to affect the calculation of the band centers.

Throughout this paper, band centers and 1σ errors were calculated with the same procedure used in Burbine et al. (2018). To determine peak positions, fourth-order polynomials were first fit over the ~ 0.7 , ~ 1.5 , and $\sim 2.5 \mu\text{m}$ maxima. Linear continua (the spectral slope) over Bands I and II were then divided out using the maxima as tangent points. The bottom one-third of Band I was then fit with a fourth-order polynomial, and the bottom one-third of Band II was fit with a second-order polynomial. The wavelength positions of the band minima were then determined. All reflectance values for the asteroid spectra were then randomly resampled using a Gaussian distribution based on the 1σ uncertainty for each reflectance value. The resampling produces a new spectrum, which was then fit. This resampling was done 99,999 times for each band. A mean band minimum and a standard deviation for each band center were then determined (Table 1). As expected, the band centers move to shorter wavelengths with decreasing Fe and Ca contents of the pyroxenes.

Element mapping and quantitative analysis were done using the Cameca SXfive-Tactis electron probe microanalyzer at the University of Massachusetts Amherst with Cameca’s Peaksight 6.4 control and automation software. Thin sections were carbon coated (25 nm thickness) using thermal vacuum evaporation prior to analysis. Mapping was done using a 15 kV , 100 nA electron beam with a $5 \mu\text{m}$ beam diameter. Elements included Al (Al $K\alpha$), Fe (Fe $K\alpha$), Ca (Ca $K\alpha$), Mg (Mg $K\alpha$), and Si (Si $K\alpha$), all via wavelength dispersive spectrometers (WDSs). Maps used a $20 \mu\text{m}$ step size with pixel dimensions sufficient to cover the sample. Pixel dwell time was 40 ms . Quantitative analysis of pyroxenes was done with a 15 kV , 40 nA beam with a $1 \mu\text{m}$ beam diameter. Analyses were done for Na, Mg, Ca, Al, Si, K, Ti, Mn, and Fe using WDS, including calibration on appropriate silicate and oxide standards. Acquisition times were 30 s except for Na (10 s) and K (20 s). Approximately 100 points were analyzed (at random) from pyroxenes, as identified from maps, in each section. Data were limited to those with totals between 99% and 101% .

The average bulk Fs and Wo contents for these three HEDs are given in Table 2. The measured bulk pyroxene compositions are consistent with previous analyses. Data for pyroxenes from ALH 76005 confirm that it is a polymict eucrite with Mg#s ranging from approximately 66 down to 36 and Wo

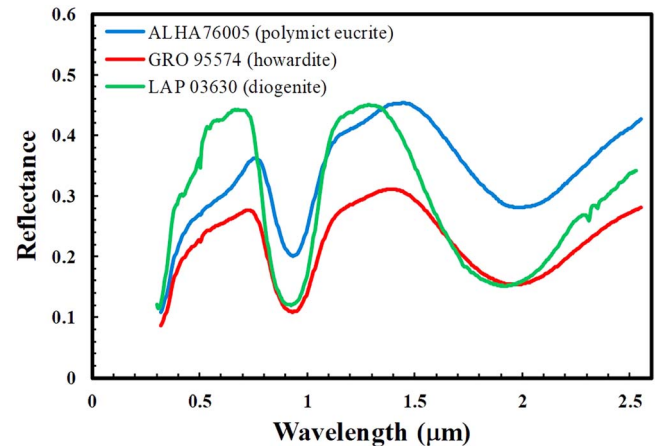


Figure 4. Reflectance spectra of polymict eucrite ALHA76005 (blue line), howardite GRO 95574 (red line), and diogenite LAP 03630 (green line). All of the meteorite reflectance spectra were acquired at RELAB. The spectrum of LAP 03630 has a number of slight absorption features in the visible and at $\sim 2.3 \mu\text{m}$, which may be due to terrestrial weathering and/or contamination from plastic from the vial. The particle sizes of the meteorites are $25\text{--}125 \mu\text{m}$.

contents ranging up to 45. No examples of diogenitic materials were present among the grains analyzed. Data for pyroxenes from GRO 95574 range in Mg# from 78 down to 38, with some analyses having Wo contents up to 44, indicating augite exsolution lamellae within low-Ca pyroxene. This meteorite is a howardite with a significant ($\sim 50\%$) diogenitic component. Data for LAP 03630 confirm that it is a diogenite with a very uniform Mg# of approximately 75. The uniformity of the Mg# for LAP 03630 is apparent by the extremely small uncertainties for its Fs and Wo contents.

Not enough meteorites were analyzed to calculate any meaningful statistics. However, even with a controlled study, some of the predicted bulk pyroxene compositions vary from the measured bulk pyroxene compositions. One possible explanation for these differences is the heterogeneous nature of many eucrites and howardites. A $\sim 10\text{--}100 \text{ mg}$ sample may have a slightly to a significantly different bulk composition than a thin section of the same meteorite. To test these formulae, a large number of HED spectra must be studied.

2.2. Meteorite Spectra

To test how well these formulae work, we first downloaded over 300 HED reflectance spectra from the RELAB database. All spectra were of powdered samples. Some meteorites had multiple spectra. We determined the band centers from the spectra; used the formulae to determine their Fs and Wo contents from their Band I and Band II centers, respectively; and then determined their bulk pyroxene compositions by averaging the derived Fs and Wo contents, respectively. For spectra without reflectance uncertainties, we assumed that their

Table 2
The Measured Fs (mol%) and Wo (mol%) Contents versus the Calculated Fs and Wo Contents

Meteorite	Measured (mol%)		Band I Formulae (mol%)		Band II Formulae (mol%)		Final Averaged (mol%)	
	Fs	Wo	Fs	Wo	Fs	Wo	Fs	Wo
LAP 03630	24.4 ± 0.2	2.3 ± 0.1	28.0	3.9	20.6	1.2	24.3	2.6
GRO 95574	32.2 ± 11.5	6.1 ± 12.3	42.5	9.6	36.5	7.3	39.5	8.5
ALHA76005	48.8 ± 10.5	13.8 ± 11.4	48.1	11.8	45.2	10.6	46.6	11.2

Note. As discussed later in this paper, there is a ± 3 mol% uncertainty for the final predicted averaged Fs content and a ± 2 mol% uncertainty for the final predicted averaged Wo content.

reflectance uncertainties were 0.005. We removed any spectra from the data set that had anomalous band centers compared to HEDs and/or would not be classified as a V-type. We also removed any spectra that appeared to be taken of samples with a considerable amount of impact melt. For example, we removed the spectra of one eucrite (NWA 5218) that had anomalous Band II centers and contained a considerable amount of impact melt (Wittmann et al. 2011). We ended up with 307 HEDs to analyze. Of the 307 total HED spectra, 17% were diogenites, 36% were howardites, and 47% were eucrites. Classifications were from the Meteoritical Bulletin Database (2023), except for EET 87532 and QUE 97002, which were reclassified (Righter 2022) as howardites from their original classifications as polymict eucrites. Of the eucrites, 15% were classified as brecciated, 3% as cumulate, 6% as Mg-rich, 19% as monomict, 45% as polymict, 10% as unbrecciated, and 2% just as eucrites with no subtype. We include a clast from the polymict eucrite Macibini as part of the polymict eucrites.

The distribution of HED band centers (Table A1 in Appendix A) falls on a relatively linear trend (Figure 5). Band center analysis (Figure 5) is clearly an effective method of discriminating between the component HED lithologies (howardites, eucrites, diogenites). However, there is some overlap between the howardites, eucrites, and diogenites. Two HEDs fall far from the trend. The diogenite that plots to the far left is GRA 98108, which is a bulk powder and has a very blue spectral slope. The fitting of this HED with a very blue spectral slope appears to result in a very short Band I center. The eucrite that plots at the far upper right of the plot is unbrecciated eucrite MAC 02522 with a grain size less than 45 μm . The long band centers for this meteorite appear to be due to its pyroxenes being extremely Fe- and Ca-rich ($\text{Fs}_{38-51}\text{Wo}_{12-30}$; McBride et al. 2003b).

“Anomalous” eucrites Ibitira, Pasamonte, and PCA 91007 all have band centers that fall on the HED trend (Appendix A). This result is consistent with the analyses of Mittlefehldt et al. (2022), who found that eucrite-like meteorites with “anomalous” oxygen isotopic compositions can have typical eucritic petrologies. They argue that different parent bodies can produce basalts with extremely similar mineralogies.

To test the formulae, we estimated average pyroxene compositions for as many HEDs with reflectance spectra as possible (Table B1 in Appendix B). These 61 HEDs had either a published bulk pyroxene composition or unpublished analyses that we could use to calculate a meaningful bulk average. Thirteen of these HEDs were used in deriving the Burbine et al. (2018) formulae. We used a wide variety of sources such as Steele & Smith (1976), Harlow et al. (1979), Takeda et al. (1981), the Basaltic Volcanism Study Project (1981), Berkley & Boynton (1992), Yamaguchi et al. (1993),

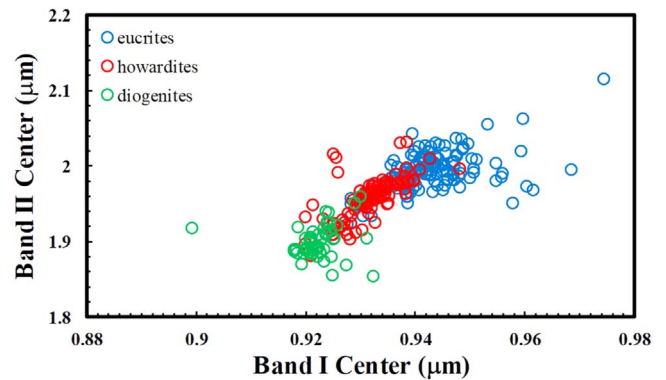


Figure 5. The distribution of calculated band centers (μm) for the howardites (red circles), eucrites (blue circles), and diogenites (green circles). The diogenite that plots to the far left is GRA 98108, which is a bulk powder. The eucrite that plots to the far right is MAC 02522 ($<45 \mu\text{m}$). The error bars for the meteorite spectra are not plotted since they are smaller than the points.

Buchanan (1995), Zema et al. (1997, 1999), Buchanan et al. (2000b), Kojima & Yamaguchi (2005), Abdu et al. (2007), Beck & McSween (2010), *Antarctic Meteorite Newsletters*, and the newly measured HEDs in this paper. Paul Buchanan has also compiled electron microprobe analyses for a number of HEDs. Some of these unpublished data were used in Buchanan et al. (2000a) and Burbine et al. (2001, 2007, 2009, 2018). Analytical techniques for the unpublished data are similar to those given in Buchanan & Mittlefehldt (2003).

We found that 156 of the HED reflectance spectra had corresponding bulk pyroxene compositions; however, 13 of the spectra were used in deriving the Burbine et al. (2018) formulae. The spectra were all for bulk meteorites except for a clast from the polymict eucrite Macibini, for which we have detailed compositional analyses. We compared the bulk pyroxene compositions calculated from their reflectance spectra using the Burbine et al. (2018) formulae with the estimated bulk pyroxene composition of each HED. A small number of the calculated bulk pyroxene compositions from the Band I and/or Band II center formulae were physically impossible because they resulted in either negative Wo contents or total Fs and Wo contents greater than 100%. Due to the nature of the formulae, band centers at very short wavelengths had negative Wo contents, while band centers at very long wavelengths could have total Fs and Wo contents greater than 100%.

We found that the best estimates of the Fs and Wo contents of the HEDs were calculated by averaging the values calculated from the Band I and Band II formulae, respectively. For the set of 143 HED spectra, which does not include those spectra used in deriving the Burbine et al. (2018) formulae, the average

absolute values of the differences between Fs and Wo values estimated from the meteorite spectra and from thin sections were ± 3.2 mol% for the predicted Fs content and ± 2.0 mol% for the predicted Wo content. Rounding these numbers results in a ± 3 mol% uncertainty for the predicted Fs content and ± 2 mol% uncertainty for the predicted Wo content. For the full set of 156 HED spectra, the average absolute values of the differences between Fs and Wo values estimated from the meteorite spectra and from thin sections were ± 3.2 mol% for the predicted Fs content and ± 1.9 mol% for the predicted Wo content.

Beck et al. (2011) have argued that the Burbine et al. (2007, 2009) formulae significantly overestimate the Fs and Wo contents. To test the Burbine et al. (2018) formulae, we examined whether there were any systematic differences between the calculated and average Fs and Wo contents by looking at the average of the differences (the predicted Fs content minus the actual Fs content and the predicted Wo content minus the actual Wo content) and not the absolute value of the differences. A positive value will mean an average overestimation using the formulae, and a negative value will mean an average underestimation using the formulae. For the set of 143 HED spectra, which does not include those spectra used in deriving the Burbine et al. (2018) formulae, the average values of the differences between the Fs and Wo values estimated from the meteorite spectra and from thin sections were $+1.1$ mol% for the predicted Fs content and $+1.2$ mol% for the predicted Wo content. For the full set of 156 HED spectra, the average values of the differences between the Fs and Wo values estimated from the meteorite spectra and from thin sections were $+1.0$ mol% for the predicted Fs content and $+1.1$ mol% for the predicted Wo content. We found no significant average overestimation of the predicted Fs and Wo contents, respectively, when using the Burbine et al. (2018) formulae since these systematic differences are smaller than the calculated uncertainties.

The Burbine et al. (2018) formulae were originally derived for Band I centers that ranged from 0.92 to $0.95 \mu\text{m}$ and Band II centers that ranged from 1.89 to $2.025 \mu\text{m}$. Looking at the distribution of band centers for the HEDs, we estimate that the formulae are valid for Band I centers between ~ 0.92 and $\sim 0.96 \mu\text{m}$ and Band II centers between ~ 1.88 and $\sim 2.03 \mu\text{m}$. A Band I center of 0.92 and a Band II center of $1.88 \mu\text{m}$ result in a $\text{Fs}_{23}\text{Wo}_2$ composition, which is consistent with the bulk pyroxene mineralogy of diogenites. A Band I center of $0.95 \mu\text{m}$ and a Band II center of $2.03 \mu\text{m}$ result in a $\text{Fs}_{57}\text{Wo}_{15}$ composition, which is at the high end of the pyroxene compositions that can be found in eucrites.

Figure 6 plots the distribution of predicted Fs content versus predicted Wo content for all the HED spectra. The predicted pyroxene compositions are the Fs and Wo contents calculated from the band centers. Predicted pyroxene compositions that are physically impossible are circled. As expected, the predicted Fs and Wo contents fall on a linear trend since the predicted pyroxene compositions are the average of two linear equations.

As can be seen from Figure 5, diogenites tend to dominate predicted pyroxene contents that are less than or equal to $\sim \text{Fs}_{28}\text{Wo}_4$. Howardites tend to dominate predicted pyroxene contents from $\sim \text{Fs}_{35-41}\text{Wo}_{7-9}$. Noncumulate eucrites tend to dominate predicted pyroxene contents that are greater than or equal to $\sim \text{Fs}_{46}\text{Wo}_{11}$. Howardites and diogenites tend to overlap

for predicted pyroxene contents of $\sim \text{Fs}_{29-34}\text{Wo}_{5-6}$, and eucrites and howardites tend to overlap for predicted pyroxene contents of $\sim \text{Fs}_{42-45}\text{Wo}_{10}$. From the analysis of the band centers, we find that the meteorite data support classifying Vestoids using band centers as a eucrite, a eucrite/howardite, a howardite, a howardite/diogenite, or a diogenite based on the predicted pyroxene compositions. This discrimination of different HEDs based on band centers is expected based on their mineralogy (e.g., Mittlefehldt et al. 1998) and the relationship between their mineralogy and band center positions (e.g., Gaffey 1976).

2.3. V-type Spectra

Formulae for determining pyroxene contents are typically not directly applied to band centers determined from Vesta or Vestoid spectra since pyroxene band positions are known to move to shorter wavelengths with decreasing temperature (e.g., Roush & Singer 1986; Reddy et al. 2012). HED spectra are usually only measured at room temperature. Due to their distance from the Sun, main-belt objects have surface temperatures that are typically ~ 70 – 100 K lower than room temperature. The typical procedure is to apply a temperature correction to each band center position.

Asteroids are modeled as gray bodies, which have emissivities that cause them to deviate from being ideal blackbodies. The surface temperature is assumed to be a function of the object's distance from the Sun, the body's Bond albedo, and its emissivity. The Bond albedo is the fraction of total power scattered by a body. The formula for calculating the mean effective surface temperature (T) in kelvin of an asteroid is

$$T = \sqrt[4]{\frac{L_0(1-A)}{16\pi\epsilon\sigma r^2}}, \quad (5)$$

where L_0 is the solar luminosity in watts, A is the Bond albedo, ϵ is the emissivity, σ is the Stefan-Boltzmann constant, and r is the distance of the asteroid from the Sun in meters. The emissivity accounts for a body not being a perfect blackbody and is not emitting light with 100% efficiency. The emissivity of an asteroid is usually assumed to be 0.9 (Harris & Lagerros 2002).

The Bond albedo for most asteroids is not well known and is usually calculated from the visual geometric albedo, which has been determined for many asteroids from infrared observations from space. The geometric albedo is the ratio of an object's brightness at zero phase angle to a Lambertian disk with the same cross section. The Bond albedo is related to the geometric albedo by multiplying by a phase integral that accounts for scattering in all directions. Li et al. (2013) derived a Bond albedo for Vesta of 0.20 ± 0.02 . Hicks et al. (2014) calculated the Bond albedo for a composite V-type asteroid solar phase curve to be 0.15 ± 0.03 . To estimate the temperatures of the asteroids, we will use Bond albedos of 0.20 for Vesta and 0.15 for other V-type bodies since the phase integrals for most Vestoids are unknown. The effect on the surface temperature due to the Bond albedo is rather small. For example, increasing the Bond albedo from 0.15 to 0.30 only decreases the surface temperature of inner main-belt asteroids by ~ 8 – 10 K.

Using previously published reflectance spectra of a eucrite, a howardite, and a diogenite taken at a range of temperatures, Reddy et al. (2012) devised temperature corrections to Band I and Band II centers for eucrites/howardites and diogenites,

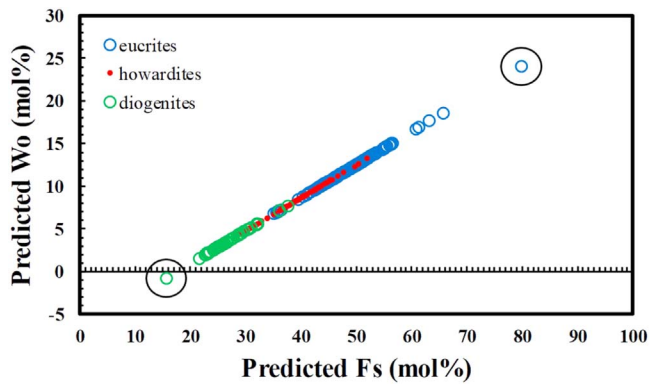


Figure 6. The distribution of predicted Fs content (mol%) vs. predicted Wo content (mol%) for the diogenites (green circles), howardites (red circles), and eucrites (blue circles). All points fall on a straight line since the Fs and Wo contents are an average of two linear equations. Due to all points falling on a straight line, we use small red circles to represent the howardites so overlapping regions can be distinguished in the plot. Predicted pyroxene compositions that are physically impossible are circled. There is a ± 3 mol% uncertainty for the predicted Fs content and a ± 2 mol% uncertainty for the predicted Wo content.

respectively. The band center corrections to room temperature for eucrites/howardites were given as

$$\text{Band I center correction } (\mu\text{m}) = 0.01656 - 0.0000552 \times T(\text{K}) \quad (6)$$

and

$$\text{Band II center correction } (\mu\text{m}) = 0.05067 - 0.00017 \times T(\text{K}). \quad (7)$$

The band center corrections to room temperature for diogenites were given as

$$\begin{aligned} \text{Band I center correction } (\mu\text{m}) &= 0.0000000017 \times T^3(\text{K}) \\ &- 0.0000012602 \times T^2(\text{K}) + 0.0002664351 \times T(\text{K}) - 0.0124 \end{aligned} \quad (8)$$

and

$$\text{Band II center correction } (\mu\text{m}) = 0.038544 - 0.000128 \times T(\text{K}). \quad (9)$$

For inner main-belt Vestoids, the correction is $\sim +0.006$ – $0.008 \mu\text{m}$ to Band I and $\sim +0.016$ – $0.022 \mu\text{m}$ to Band II for eucrite/howardite compositions. The correction is $\sim +0.004$ – $0.005 \mu\text{m}$ to Band I and $\sim +0.015$ – $0.018 \mu\text{m}$ to Band II for diogenite compositions.

3. Analysis

We have analyzed publicly available main-belt and Mars-crossing V-type bodies (Table C1 in Appendix C) that had spectra in the visible and near-infrared wavelength regions. The near-infrared reflectance spectra were all taken using SpeX at the IRTF (Hardersen et al. 2004, 2014, 2015, 2018; DeMeo et al. 2009; Moskovitz et al. 2010; Bus 2011; Hardersen 2016; Reddy & Sanchez 2016; SMASS 2023). We did not use any near-infrared spectra with extremely large reflectance error bars. The near-infrared reflectance spectra used in the DeMeo et al. (2009) taxonomy had charge-coupled device (CCD) visible spectra (Bus & Binzel 2002) already spliced to their SpeX spectra. Other V-type asteroids had visible spectra (Bus & Binzel 2003) spliced to their near-infrared spectra when necessary so the reflectance peak located at ~ 0.7 – $0.8 \mu\text{m}$

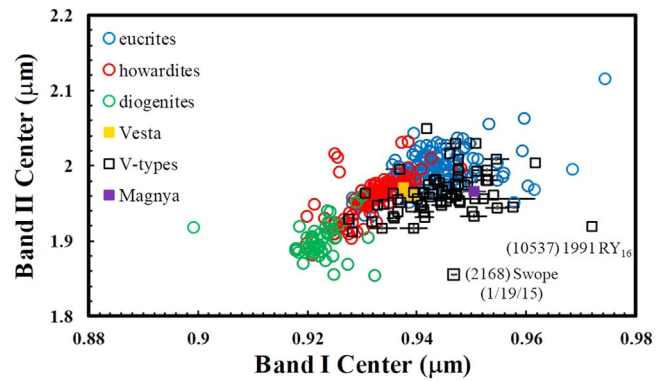


Figure 7. The distribution of band centers (μm) of the howardites (red circles), eucrites (blue circles), diogenites (green circles), the V-type asteroids (black open squares), Vesta (filled orange square), and Magnya (filled purple diamond). The asteroid band centers are corrected for temperature. The points for (2168) Swope (2015 January 19) and (10537) 1991 RY₁₆ are labeled since they plot far from the HED trend. The error bars for the meteorite spectra are not plotted since they are smaller than the points.

would be part of each analyzed spectrum. Older IRTF spectra only have wavelength coverage down to $\sim 0.8 \mu\text{m}$, while newer IRTF spectra had coverage down to $\sim 0.7 \mu\text{m}$. The CCD and IRTF spectra were spliced together by finding the average ratio of reflectance values for the same wavelength values in the CCD and SpeX spectra and multiplying the SpeX spectrum by this average ratio. We assumed reflectance uncertainties of 0.01 for all reflectances for the (1459) Magnya spectrum since that spectrum did not have listed uncertainty values. Vestoids and HEDs tend to be much redder in spectral slope than Vesta, which Buratti et al. (2013) propose could be due to the presence of dark and spectrally neutral carbonaceous material on Vesta. Fulvio et al. (2016) have argued that differences in spectral slopes among Vestoids are due to different objects experiencing different degrees of space weathering and that space weathering would be expected to redden Vestoid spectra. However, dividing out the linear continua over both Band I and Band II, respectively, should minimize the effect of reddening due to space weathering when calculating the band centers.

Band I and Band II centers were calculated from 71 V-type reflectance spectra taken of 49 bodies (Table D1 in Appendix D) in and outside the Vesta family. Sixteen bodies had multiple spectra. All asteroid band centers (Table E1 in Appendix E) were calculated using the same procedure used to calculate the band centers for the HEDs. The eucrite/howardite temperature correction (Equations (5) and (6)) was applied to all band centers since the Vestoids did not have band centers consistent with just diogenitic material. The calculated band centers from Hardersen et al. (2014, 2015, 2018) and Hardersen (2016) reflectance spectra tended to have extremely small uncertainties with values as low as 0.000 since their spectra had extremely small reflectance error bars. All band centers are listed with three significant digits since the goal is to calculate Fs and Wo contents rounded to a maximum of only two significant digits. The calculated band centers may differ from previously published band centers since we use a different fitting technique and divide out a spectral slope.

Figure 7 plots the band centers of the HEDs and asteroids, which were corrected for temperature. This type of plot of Band I versus Band II center is a common way of comparing the spectral properties of V-type asteroids to HEDs (e.g., Duffard et al. 2004, 2006; Burbine et al. 2009, 2018;

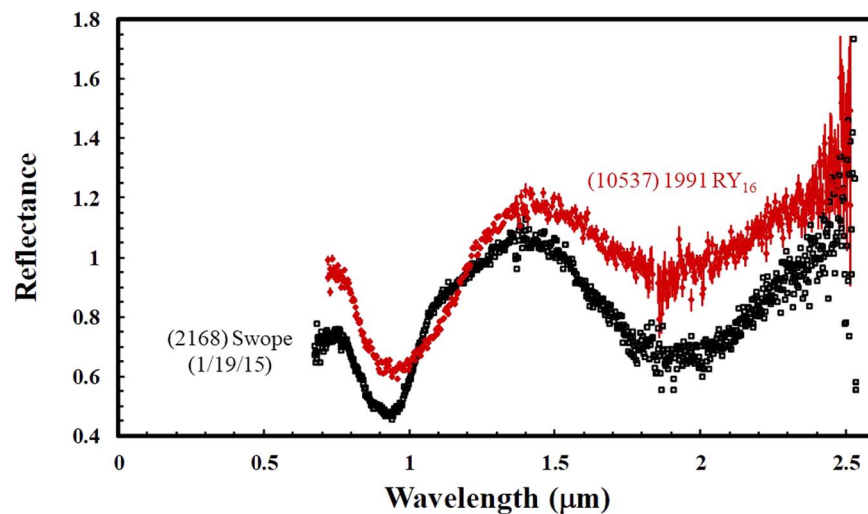


Figure 8. Reflectance spectra of (2168) Swope (2015 January 19) (black open squares) and (10537) 1991 RY₁₆ (dark-red open diamonds). The Swope IRTF spectrum is from Hardersen et al. (2018), and the 1991 RY₁₆ IRTF spectrum is from Moskovitz et al. (2010). The Swope and 1991 RY₁₆ reflectance values have not been normalized and are just the published values (Bus 2011; Hardersen 2016). The uncertainties for the asteroid reflectance spectra are 1σ .

Moskovitz et al. 2010; Mayne et al. 2011; Hardersen et al. 2014, 2015, 2018; Migliorini et al. 2017). The V-type band centers tend to overlap the values for eucrites and howardites and not the values for diogenites. From the distribution of band centers for the HEDs, the V-type asteroids have mineralogies most similar to eucrites and howardites and not diogenites. Many other researchers (Burbine et al. 2001; Moskovitz et al. 2010; Hardersen et al. 2018) have previously noticed the scarcity of diogenitic bodies among main-belt Vestoids. Burbine et al. (2009) found that diogenitic asteroids also appeared rare among near-Earth objects. However, using Modified Gaussian Modeling (MGM), which determined the relative proportions of low- and high-Ca pyroxenes, Mayne et al. (2011) found that approximately one-third of their studied Vestoids had diogenitic compositions. Migliorini et al. (2017) also found a high proportion of diogenitic compositions among the V-type asteroids observed at the Telescopio Nazionale Galileo. Using radiative transfer modeling, Angrisani et al. (2023) also found a high proportion of diogenitic compositions among their studied V-type asteroids.

The distribution for the temperature-corrected V-type band centers tends to fall slightly below the HED distribution. This offset argues that the temperature corrections might not be large enough. The calculated Fs and Wo contents would then be lower limits. The relatively simplistic temperature calculation may be significantly overestimating the asteroid surface temperatures, and their surfaces might tend to be much colder. Doubling the Bond albedo or increasing the emissivity to 1.0 does not lower the temperature enough to produce a dramatic increase in the band corrections determined from the Reddy et al. (2012) equations. Further work needs to be done to see the effect on HED band centers with decreasing temperature.

The two spectra (Figure 8) that plot far from the HED distribution are one of the three observations of (2168) Swope (which plots below the HED distribution) and the observation of (10537) 1991 RY₁₆ (which plots to the right). Asteroid 1991 RY₁₆ is located far from Vesta in the outer main belt, and its spectrum has been interpreted as having an olivine component (Moskovitz et al. 2008b; Leith et al. 2017), which would increase its Band I center value. Asteroid 1991 RY₁₆ is thought to be a fragment of a parent body in the outer part of the

asteroid belt that was partially or fully differentiated. The physical reason for the “low” Band II center value for one of the Swope spectra is not clear, so this band center is still used in the analysis.

The estimated pyroxene compositions for Vesta and the Vestoids, the interpreted mineralogy for each object, and other researcher’s interpretations are given in Table 3. For objects with multiple spectra, we averaged the pyroxene compositions. We do not list a composition for 1991 RY₁₆ owing to its anomalous Band I center that appears to be due to a “significant” olivine component.

Compared to previous analyses, our interpreted pyroxene mineralogies for the Vestoids tend to be more Fs- and Wo-rich. One possible reason for these differences is that the slopes of the four equations from Burbine et al. (2018) for determining Fs and Wo contents are steeper than the slopes for the previously derived equations from Burbine et al. (2007, 2009). The band centers of the 13 HED spectra used to derive the Burbine et al. (2018) formulae were calculated using a MATLAB program that did 100,000 fits where each spectrum is randomly resampled 99,999 times using a Gaussian distribution based on the 1σ uncertainty for each reflectance value. The HED band centers used to derive the Burbine et al. (2007, 2009) equations were determined using a much simpler fitting technique, and therefore the band centers used to derive the Burbine et al. (2018) equations should more accurately represent the “actual” band centers of the HED spectra. A steeper slope for the equations would tend to increase the derived Fs or Wo contents, respectively, with increasing Band I and II center positions. The Burbine et al. (2007, 2009) formulae were previously used to help derive the bulk pyroxene composition of Vestoids in Hardersen et al. (2014, 2015, 2018).

In contrast to the findings of this study, Migliorini et al. (2017) found, using band centers, that diogenitic V-type asteroids were not particularly rare using their spectral observations of V-type asteroids taken at the Telescopio Nazionale Galileo. However, the spectra taken at the Telescopio Nazionale Galileo tend to have a considerable amount of missing data between 1.8 and 2.0 μm owing to the telluric absorption band. These bodies that were interpreted by

Table 3
Calculated Bulk Pyroxene Compositions for Each V-type Asteroid

Asteroid	Average (mol%)		Interpretation	Previous Interpretation
	Fs	Wo		
(4) Vesta	43	10	eucrite/howardite	howardite (Hiroi et al. 1994)
(809) Lundia	51	13	eucrite	howardite/diogenite (Birlan et al. 2014); howardite (Ieva et al. 2016)
(956) Elisa	46	11	eucrite	diogenite (De Sanctis et al. 2011; Lim et al. 2011)
(1459) Magnya	50	12	eucrite	not HED (Hardersen et al. 2004)
(1468) Zomba	53	14	eucrite	
(1929) Kollaa	49	12	eucrite	cumulate eucrite (Kelley et al. 2003); mixture (Mayne et al. 2011)
(2011) Veteraniya	44	10	eucrite/howardite	howardite (\pm eucrite) (Hardersen et al. 2015)
(2045) Peking	49	12	eucrite	mixture (Mayne et al. 2011)
(2168) Swope	44	10	eucrite/howardite	howardite (\pm eucrite) (Hardersen et al. 2015)
(2371) Dimitrov	53	14	eucrite	
(2442) Corbett	45	11	eucrite/howardite	
(2511) Patterson	47	11	eucrite	
(2566) Kirghizia	44	10	eucrite/howardite	mixture (Mayne et al. 2011)
(2653) Principia	47	11	eucrite	
(2763) Jeans	54	14	eucrite	
(2795) Lepage	44	10	eucrite/howardite	
(2851) Harbin	36	7	howardite	howardite/diogenite (Moskovitz et al. 2010); diogenite (Mayne et al. 2011)
(2912) Lapalma	42	9	eucrite/howardite	mixture (Mayne et al. 2011)
(3155) Lee	32	6	howardite/diogenite	howardite/diogenite (Moskovitz et al. 2010); diogenite (Mayne et al. 2011)
(3715) Štohl	50	13	eucrite	howardite (\pm eucrite) (Hardersen et al. 2015)
(3782) Celle	42	9	eucrite/howardite	howardite (\pm eucrite) (Hardersen et al. 2018)
(3849) Incidentia	54	14	eucrite	(Hardersen et al. 2015)
(3867) Shiretoko	60	17	eucrite	eucrite (Hardersen et al. 2014)
(4038) Kristina	38	8	howardite	
(4188) Kitezeh	46	11	eucrite	mixture (Mayne et al. 2011)
(5111) Jacliff	41	9	howardite	
(5235) Jean-Loup	42	10	eucrite/howardite	howardite (Hardersen et al. 2014)
(5560) Amytis	41	9	howardite	howardite (diogenite-rich?) (Hardersen et al. 2014)
(5754) 1992 FR ₂	46	11	eucrite	
(5875) Kuga	50	12	eucrite	eucrite (Hardersen et al. 2015)
(6331) 1992 FZ ₁	42	10	eucrite/howardite	howardite (Hardersen et al. 2014)
(6976) Kanatsu	47	11	eucrite	howardite (eucrite-rich?) (Hardersen et al. 2014)
(7800) Zhongkeyuan	53	14	eucrite	
(8149) Ruff	47	12	eucrite	howardite (\pm eucrite) (Hardersen et al. 2015)
(9147) Kourakuen	49	12	eucrite	howardite (\pm eucrite) (Hardersen et al. 2015)
(9553) Colas	38	8	howardite	howardite (\pm eucrite) (Hardersen et al. 2015)
(10537) 1991 RY ₁₆	not HED	not HED (Moskovitz et al. 2008b; Leith et al. 2017; Hardersen et al. 2018)
(10666) Feldberg	47	11	eucrite	howardite (\pm eucrite) (Hardersen et al. 2015)
(15237) 1988 RL ₆	42	9	eucrite/howardite	howardite (Hardersen et al. 2015)
(17469) 1991 BT	43	10	eucrite/howardite howardite	(diogenite-rich?) (Hardersen et al. 2014)
(19165) Nariyuki	47	11	eucrite	howardite (\pm eucrite) (Hardersen et al. 2018); eucrite (Migliorini et al. 2017)
(26886) 1994 TJ ₂	39	8	howardite	howardite/diogenite (Moskovitz et al. 2010)
(27343) Deannashea	39	8	howardite	howardite/diogenite (Moskovitz et al. 2010)
(29796) 1999 CW ₇₇	47	11	eucrite	howardite (Hardersen et al. 2014)
(30872) 1992 EM ₁₇	51	13	eucrite	howardite (Hardersen et al. 2014)
(31414) Rotarysusa	41	9	howardite	diogenite (\pm howardite) (Hardersen et al. 2015)
(32940) 1995 UW ₄	54	14	eucrite	howardite (Hardersen et al. 2015)
(33881) 2000 JK ₆₆	45	11	eucrite/howardite	
(38070) Redwine	47	11	eucrite	

Note. The term “mixture” from Mayne et al. (2011) refers to either a howardite or a body with significant components of eucritic and diogenitic material. The term “ \pm eucrite” from Hardersen et al. (2015) means a possible enhancement in the eucritic component, and the term “ \pm howardite” means a possible enhancement in the howarditic component.

Migliorini et al. (2017) as being diogenitic will hopefully be observed again.

It is unclear why Mayne et al. (2011) and Angrisani et al. (2023) found a higher percentage of diogenitic objects than our study since all three studies used many of the same bodies. Further work needs to be done to understand why using band

centers produces different results from methods that fit or model the absorption bands. The formulae for determining pyroxene mineralogies used in this paper were tested using hundreds of HED spectra, and a large mineralogical test needs to be done with the methods used by Mayne et al. (2011) and Angrisani et al. (2023).

We calculate a bulk pyroxene mineralogy for Magnya that is consistent with eucrites, which is different from the interpretation of Hardersen et al. (2004). Our calculated band centers for Magnya are longer than those calculated by Hardersen et al. (2004). This discrepancy may be due to the result of dividing out a spectral slope when deriving the band centers for Magnya in this paper. Hardersen et al. (2004) also used equations from Gaffey et al. (2002) for determining the pyroxene mineralogy. Magnya is located far from Vesta and appears dynamically difficult to derive from Vesta (Michtchenko et al. 2002).

Excluding Vesta, Magnya, and 1991 RY₁₆, we find that 54% of the remaining V-type asteroids had predicted Fs and Wo contents consistent with eucrites, 26% with eucrites/howardites, 17% with howardites, and 2% with howardites/diogenites. To make these predictions, we use the previously defined Fs and Wo ranges for the HEDs that we discussed earlier in the paper. If an object had a predicted Fs or a predicted Wo content that fell in the range of one of the overlapping classes (howardite/diogenite or eucrite/howardite), the object was given one of these overlapping class designations. The scarcity of diogenitic Vestoids indicates that it may be extremely difficult to excavate kilometer-sized bodies with surfaces of 90 mol% or more of diogenitic material from Vesta.

Eucrites (including polymict eucrites) also dominate HED falls (57% of HED falls) and all recovered HED material (falls and finds) (62%; Meteoritical Bulletin Database 2023). Diogenites are 17% of HED falls and 22% of all recovered HED material, while howardites are 26% of HED falls and 16% of all recovered HED material. However, fall statistics and find statistics will be biased toward more coherent material that can withstand entry into Earth's atmosphere.

A size dependence is also apparent among HED meteorites. The largest known masses of a howardite (Lohawat) and a diogenite (Johnstown) are both ~40 kg. Both Lohawat and Johnstown are falls. However, there are 10 eucrites (falls and finds) with masses greater than 40 kg. The Millbillillie eucrite has an estimated mass of ~330 kg, and the Jikharra 001 eucrite-melt breccia had at least 2.5 metric tons recovered (Meteoritical Bulletin Database 2023). The reason for this size discrepancy on a smaller scale than the Vestoid sizes could be due to larger eucritic fragments just being more common in space. Eucrites may be stronger than howarditic and diogenitic material. Howardites are breccias, so they might be expected to be weaker than eucrites and therefore easier to break apart in space.

Dawn observations (De Sanctis et al. 2012, 2013; Ammannito et al. 2013a; McSween et al. 2013a, 2019) found that diogenitic material is much less abundant on the surface of Vesta than eucritic and howarditic material but did identify some exposures of diogenitic material in the Rheasilvia basin. Combe et al. (2015) also found that diogenitic ejecta from the Rheasilvia basin reached the northern hemisphere of Vesta. Impacts on Vesta would have mixed diogenitic material with the eucritic crust but appear not to have ejected relatively large fragments with significant surface abundances (90 mol% or greater) of diogenitic material. Diogenitic material is still present on the surfaces of Vestoids but in abundances less than 90 mol%.

The scarcity of olivine diogenites (Shearer et al. 2010) and possible Vestan olivine-rich fragments (Vaci et al. 2021) in meteorite collections is consistent with impacts that tended not

to excavate deep into the mantle. The Rheasilvia basin has an estimated depth of only ~20 km (Schenk et al. 2012). Olivine-rich exposures are relatively rare on the surface of Vesta (Ammannito et al. 2013b; McSween et al. 2013a) and tend not to be found at its south pole. Due to the absence of large exposures of diogenitic and olivine-dominated material on Vesta, Jutzi et al. (2013) argue that Vesta could have a ~100 km thick basaltic crust with diogenitic intrusions (sills) or that the outer ~100 km is well mixed by collisions. Using results from melting models, Mitchell et al. (2021) also argued that diogenites formed as intrusions into a eucritic crust.

One big unknown is the internal structure of the Vestoids. Davis et al. (2002) found that the estimated percentage of rubble piles among asteroids ~5–10 km in diameter varied greatly depending on the reaccumulation model. HEDs have an average bulk density of 2.90 g cm⁻³ and an average porosity of 10.5% (Macke et al. 2011). Without knowing the density of the Vestoids, which would allow an estimation of the amount of pore space, it is not possible to know the internal structure of the Vestoids. Vesta is usually assumed to be a protoplanet that is relatively intact (Jutzi et al. 2013) owing to having a eucritic crust, but it is not known whether the crust is relatively intact or a rubble pile. From the absence of a systematic pattern of scarps and ridges where the Rheasilvia basin overlays the Veneneia basin, Cheng & Klimczak (2022) argue that the outer part of Vesta has been shattered.

If the Vestoids are relatively intact fragments of Vesta's crust, Vesta's crust would be expected to also be relatively intact. The lack of diogenitic Vestoids but the significant abundance of diogenitic meteorites could be due to diogenitic material intruding into Vesta's crust and having relatively small thicknesses (Figure 9). Modeling by Wilson & Keil (1996) suggested that "deep" intrusions (sills) on Vesta would have had thicknesses of only 3 m or less. The best terrestrial analog for these intrusions is probably the multikilometer-thick mafic-ultramafic Stillwater complex (e.g., Jenkins et al. 2021); however, the gravity regimes on Earth and Vesta are vastly different, so it is extremely difficult to directly compare thicknesses. These diogenitic melts would have intruded into the eucritic crust (e.g., Barrat et al. 2010; Clenet et al. 2014). Since diogenites tend to be relatively coarse grained (Mittelfeldt 2015), we would assume that these sills would have intruded into very hot country rocks and would have cooled very slowly to produce their relatively coarse grain sizes. If diogenitic regions in the eucritic crust were not very thick, then the formation of craters on Vesta would have only produced "small" diogenite fragments that could have only come to Earth as meteorites. Diogenitic bodies would not be observed since diogenitic Vestoids would not be large enough to be characterized from Earth. These "thin" diogenitic intrusions must have formed as part of an extensive network on Vesta for diogenites to consistently fall to Earth and be abundant components of howardites. The relative abundance of diogenitic material in meteorite collections but the rarity of diogenitic exposures on the surface of Vesta would argue against a model where diogenites only existed below the eucritic crust.

If the Vestoids are primarily rubble piles, Vesta's eucritic crust and part of the lower diogenitic layer may have been shattered and then reassembled. Diogenitic fragments would then be mixed with the eucritic crust. Impacts would then have released fragments that are primarily eucritic or howarditic since diogenitic rubble in the crust would be expected to be at

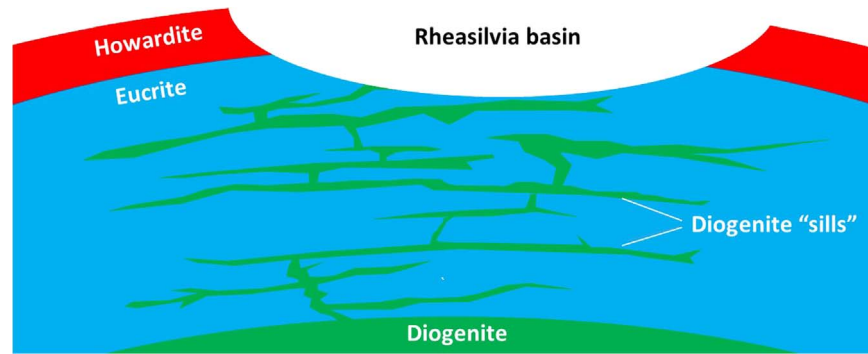


Figure 9. Cartoon of possible stratigraphy of Vesta’s crust. Relatively thin diogenitic sills (green color) would intrude into the eucritic crust (blue color). The top surface would be a mixture of eucritic and diogenitic material (howarditic) (red color). The impact that formed the Rheasilvia basin would have ejected a considerable amount of HED material into space. The Rheasilvia basin is not drawn to scale since it has a diameter of ~500 km and a depth of ~20 km (Schenk et al. 2012).

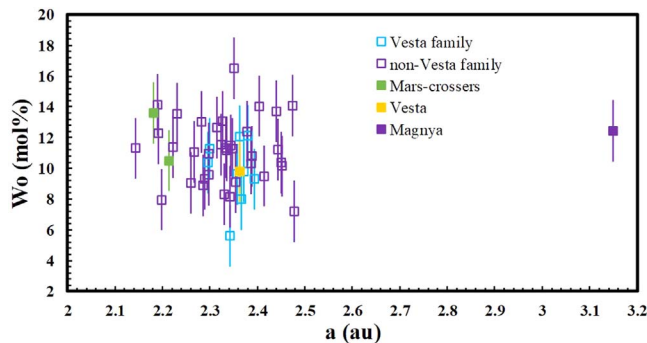


Figure 10. The derived Wo contents (mol%) vs. semimajor axis a (au) for all the V-type bodies (excluding 1991 RY₁₆). Vesta family members are plotted with open aquamarine squares, non-Vesta family members (excluding Mars crossers) are plotted with open purple squares, and Magnya is plotted with a filled purple diamond. Mars crossers are plotted with olivine green squares, and Vesta is plotted with a filled orange square. Magnya ($a = 3.15$ au) is located far from Vesta in the outer belt.

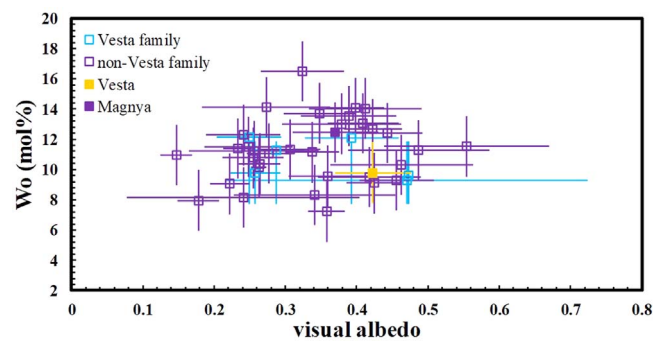


Figure 12. The derived Wo contents (mol%) vs. visual geometric albedo for the V-type asteroids (excluding 1991 RY₁₆). Visual geometric albedos are primarily from NEOWISE (Mainzer et al. 2016) except for Vesta and Magnya. Vesta’s albedo is from IRAS observations (Tedesco et al. 2004). Magnya’s albedo is from Delbo et al. (2006). For objects with multiple NEOWISE albedos, we use the albedos that have the lowest uncertainties. Vesta family members are plotted with open aquamarine squares, non-Vesta family members (excluding Mars crossers) are plotted with open purple squares, Vesta is plotted with a filled orange square, and Magnya is plotted with a filled purple square. Except for Vesta and Magnya, we do not plot objects without NEOWISE albedos (such as the Mars crossers).

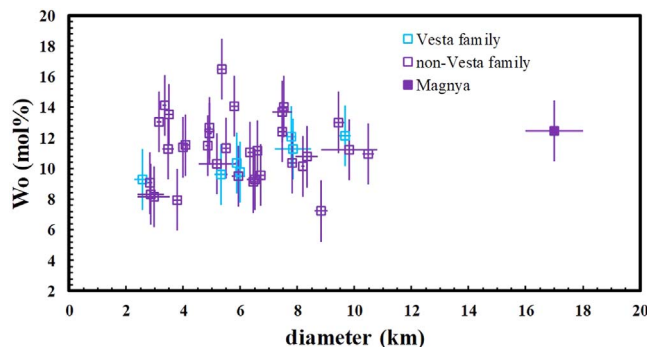


Figure 11. The derived Wo contents (mol%) vs. diameter (km) for the main-belt V-type asteroids (excluding Vesta and 1991 RY₁₆). Diameters are primarily from NEOWISE (Mainzer et al. 2016). Magnya’s diameter is from Delbo et al. (2006) and is much larger than other V-type asteroids. For objects with multiple NEOWISE diameters, we use the diameters that have the lowest uncertainties. Vesta family members are plotted with open aquamarine squares, non-Vesta family members (excluding Mars crossers) are plotted with open purple squares, and Magnya is plotted with a filled purple square. Vesta is not plotted owing to its large size. Except for Magnya, we do not plot objects without NEOWISE diameters, which includes the Mars crossers.

abundances much less than the eucritic material. The size distributions of fragments from a number of asteroid families are more consistent with breakups of pre-shattered bodies (Michel et al. 2003, 2004), which may argue that most large asteroids are rubble piles.

Table D1 in Appendix D lists the semimajor axis, membership in the Vesta family, status as a Mars crosser, diameter, and visual geometric albedo. Only asteroids (1468) Zomba and (33881) 2000 JK66 are Mars crossers. Diameters and visual geometric albedos are from Near-Earth Object Wide-field Infrared Survey Explorer (NEOWISE) observations (Mainzer et al. 2016) except for Vesta and Magnya. Vesta’s diameter is from Dawn observations (Russell et al. 2012), and its albedo is from Infrared Astronomical Satellite (IRAS) observations (Tedesco et al. 2004). Magnya’s albedo and diameter are from Delbo et al. (2006). We use the Delbo et al. (2006) values for Magnya since the NEOWISE albedo (0.909) for Magnya is extremely high. Besides Vesta and Magnya, all of the observed Vestoids had estimated diameters of 11 km or less.

We plot the derived Wo contents versus semimajor axis a (au; Figure 10) for all the V-type bodies (excluding 1991 RY₁₆). We use the derived Wo contents to represent the bulk pyroxene composition since the Wo content has smaller uncertainties than the derived Fs content and the Wo content is also directly correlated with the Fs content. There is no obvious correlation with distance from the Sun and Wo content. Vesta does plot somewhat near the middle of the Wo distribution. We see no obvious difference in the distribution of Wo contents for Vesta family members and nonfamily members.

We also plot the derived Wo contents versus diameter (km; Figure 11) and visual albedo (Figure 12) for the V-type asteroids (excluding 1991 RY₁₆). Due to Vesta's large size, we do not plot Vesta in Figure 11. Not all objects have calculated diameters and albedos. There are no obvious correlations between predicted pyroxene composition versus diameter or albedo, respectively. Outer belt object Magnya does have a much larger diameter than the other V-type asteroids. Magnya's much larger size compared to the other V-type asteroids would also argue that it is not a fragment of Vesta. The absence of a trend with pyroxene composition and asteroid albedo is consistent with the albedo values compiled by Ostrowski & Bryson (2019), where the average albedos for howardites (0.30), eucrites (0.32), and diogenites (0.29) are approximately the same.

We find no obvious relationship between semimajor axis, diameter, or albedo and pyroxene composition for the Vestoids. The impact events on Vesta appear to have ejected fragments randomly with a variety of different velocities and sizes.

4. Conclusions

We have tested the Burbine et al. (2018) equations to determine how well they can calculate bulk pyroxene compositions for HED-like material from band centers derived from their reflectance spectra. Using HEDs with known bulk pyroxene compositions, we calculated that the uncertainty in the predicted Fs contents was ± 3 mol% and the uncertainty in the predicted Wo contents was ± 2 mol%. We have used the Burbine et al. (2018) formulae to calculate the bulk pyroxene composition of a number of V-type asteroids with near-infrared spectra taken at the IRTF.

We found that diogenitic Vestoids appear extremely rare while eucritic and howarditic Vestoids appear much more common. However, diogenites are much more common among the HEDs that fall to Earth. One possible reason for this discrepancy is that diogenitic intrusions are extremely "thin" (Wilson & Keil 1996) but widespread in Vesta's eucritic crust. After impacts on Vesta, diogenitic material would be ejected as small fragments but not as multikilometer diogenitic bodies that can be observed from Earth. Another possible reason for this discrepancy is that Vesta's crust has been shattered and diogenitic material is much less common than eucritic material in the crust. Knowing the physical nature of Vestoids would

give insight into which of these two possibilities is correct. If Vestoids are intact fragments of Vesta's crust, we would expect that Vesta's upper crust is relatively intact. Since asteroid families are thought to be due to the breakups of pre-shattered bodies (Michel et al. 2003, 2004), we believe that it is more likely that Vesta's crust is shattered and Vestoids are rubble piles.

T.H.B. would like to thank the Remote, In Situ, and Synchrotron Studies for Science and Exploration 2 (RISE2) Solar System Exploration Research Virtual Institute (SSERVI) (NASA grant 80NSSC19M0215) for support. T.H.B. would also like to thank a Research Support Fund grant from UMASS Amherst that funded the electron microprobe analyses. T.H.B. would like to thank the Meteorite Working Group for approving the meteorite request. US Antarctic meteorite samples are recovered by the Antarctic Search for Meteorites (ANSMET) program, which has been funded by NSF and NASA, and characterized and curated by the Department of Mineral Sciences of the Smithsonian Institution and Astro-materials Curation Office at NASA Johnson Space Center. This research utilizes meteorite reflectance spectra acquired at the NASA RELAB facility at Brown University. The authors would like to thank Takahiro Hiroi for acquiring the newly measured HED spectra. CCD and IRTF spectra were downloaded from both the NASA Planetary Data Systems (PDS) and the Small Main-Belt Asteroid Spectroscopic Survey (SMASS) websites. Part of the data utilized in this publication were obtained and made available by the MIT-Hawaii Near-Earth Object Spectroscopic Survey (MITHNEOS). The IRTF is operated by the University of Hawaii under contract 80HQTR19D0030 with the National Aeronautics and Space Administration. The MIT component of this work is supported by NASA grant 80NSSC18K0849. DeMeo also made available the spectra that were used in formulating the Bus-DeMeo taxonomy. This research has made use of the Small Bodies Data Ferret (<https://sbnapps.psi.edu/ferret/>), which is supported by the NASA Planetary Data System. The authors would like to thank the anonymous reviewers for their insightful comments that greatly improved the manuscript.

Appendix A HED Meteorite Spectra

Table A1 lists the HED meteorite spectra analyzed in this study. We list the meteorite name, its classification, the particle size, the calculated band centers, and RELAB ID for the spectrum. We group the meteorites by classification. We use the abbreviation *diogenite-an* for an anomalous diogenite, *diogenite-olivine* for an olivine diogenite, *eucrite-br* for a brecciated eucrite, *eucrite-cm* for a cumulate eucrite, *eucrite-Mg-rich* for a Mg-rich eucrite, *eucrite-mmict* for a monomict eucrite, *eucrite-pmict* for a polymict eucrite, and *eucrite-unbr* for an unbrecciated eucrite.

Table A1
Meteorite Spectra Used in this Study

Meteorite	Class	Particle Size	Centers		RELAB ID
			Band I (μm)	Band II (μm)	
A-881526	diogenite	<25 μm	0.921 \pm 0.002	1.887 \pm 0.002	MP-TXH-095-A
ALHA77256	diogenite	<25 μm	0.925 \pm 0.001	1.880 \pm 0.002	MP-TXH-071-A
ALHA77256	diogenite	<45 μm	0.920 \pm 0.002	1.892 \pm 0.002	RM-REM-123-A
ALHA77256	diogenite	bulk	0.919 \pm 0.003	1.870 \pm 0.001	RM-REM-123-P
ALHA77256	diogenite	bulk	0.924 \pm 0.015	1.941 \pm 0.015	DD-MDD-174
ALH 85015	diogenite	<45 μm	0.924 \pm 0.003	1.938 \pm 0.003	RM-REM-122-A
ALH 85015	diogenite	bulk	0.918 \pm 0.007	1.919 \pm 0.004	RM-REM-122-P
EETA79002	diogenite	<25 μm	0.921 \pm 0.003	1.901 \pm 0.004	MB-TXH-067-G
EETA79002	diogenite	<25 μm	0.921 \pm 0.002	1.892 \pm 0.003	MB-TXH-067-A
EETA79002	diogenite	25–45 μm	0.920 \pm 0.003	1.893 \pm 0.003	MB-TXH-067-B
EETA79002	diogenite	45–75 μm	0.921 \pm 0.004	1.889 \pm 0.003	MB-TXH-067-C
EETA79002	diogenite	75–125 μm	0.920 \pm 0.005	1.889 \pm 0.003	MB-TXH-067-D
EET79002	diogenite	125–250 μm	0.921 \pm 0.005	1.898 \pm 0.004	MB-TXH-067-E
EETA79002	diogenite	<150 μm	0.921 \pm 0.003	1.903 \pm 0.003	MB-TXH-067-H
EETA79002	diogenite	250–500 μm	0.921 \pm 0.005	1.883 \pm 0.004	MB-TXH-067-F
EET 83246	diogenite	<45 μm	0.922 \pm 0.002	1.894 \pm 0.002	RM-REM-127-A
EET 83246	diogenite	bulk	0.932 \pm 0.003	1.854 \pm 0.002	RM-REM-127-P
Ellemeet	diogenite	<25 μm	0.924 \pm 0.002	1.913 \pm 0.003	MP-D2M-113
Ellemeet	diogenite	bulk	0.924 \pm 0.003	1.916 \pm 0.002	MP-D2M-112
GRA 98108	diogenite	<45 μm	0.921 \pm 0.002	1.914 \pm 0.002	RM-REM-125-A
GRA 98108	diogenite	<45 μm	0.923 \pm 0.002	1.886 \pm 0.002	MT-AWB-169-A
GRA 98108	diogenite	bulk	0.921 \pm 0.002	1.884 \pm 0.002	MT-AWB-169
GRA 98108	diogenite	bulk	0.899 \pm 0.012	1.918 \pm 0.003	RM-REM-125-P
Johnstown	diogenite	<25 μm	0.918 \pm 0.003	1.890 \pm 0.003	MB-TXH-095-A
Johnstown	diogenite	25–45 μm	0.918 \pm 0.003	1.890 \pm 0.002	MB-TXH-095-B
Johnstown	diogenite	<75 μm	0.923 \pm 0.003	1.885 \pm 0.001	MS-JTW-049-A
LAP 02216	diogenite	<45 μm	0.920 \pm 0.001	1.905 \pm 0.000	RM-REM-129-A
LAP 02216	diogenite	bulk	0.918 \pm 0.003	1.885 \pm 0.002	RM-REM-129-P
LAP 03630	diogenite	25–125 μm	0.922 \pm 0.004	1.880 \pm 0.000	TB-THB-157
LAP 03979	diogenite	<45 μm	0.926 \pm 0.002	1.922 \pm 0.002	RM-REM-131-A
LAP 03979	diogenite	bulk	0.931 \pm 0.008	1.904 \pm 0.002	RM-REM-131-P
LAP 91900	diogenite	<25 μm	0.923 \pm 0.002	1.904 \pm 0.002	MP-TXH-077-A
LAP 91900	diogenite	bulk	0.927 \pm 0.004	1.869 \pm 0.003	TB-RPB-018
LEW 88008	diogenite	<45 μm	0.920 \pm 0.002	1.885 \pm 0.000	RM-REM-128-A
LEW 88008	diogenite	bulk	0.923 \pm 0.003	1.874 \pm 0.002	RM-REM-128-P
MET 00436	diogenite	<125 μm	0.924 \pm 0.005	1.910 \pm 0.002	TB-MDD-261
MET 01084	diogenite	<45 μm	0.921 \pm 0.002	1.906 \pm 0.002	RM-REM-132-A
MET 01084	diogenite	bulk	0.918 \pm 0.003	1.887 \pm 0.002	RM-REM-132-P
MIL 03368	diogenite	<45 μm	0.922 \pm 0.003	1.910 \pm 0.001	RM-REM-121-A
MIL 03368	diogenite	bulk	0.923 \pm 0.003	1.890 \pm 0.001	RM-REM-121-P
PCA 02008	diogenite	<45 μm	0.924 \pm 0.002	1.926 \pm 0.002	RM-REM-130-A
PCA 02008	diogenite	bulk	0.923 \pm 0.003	1.919 \pm 0.002	RM-REM-130-P
QUE 99050	diogenite	<45 μm	0.920 \pm 0.001	1.891 \pm 0.002	RM-REM-120-A
QUE 99050	diogenite	bulk	0.925 \pm 0.002	1.855 \pm 0.001	RM-REM-120-P
Tatahouine	diogenite	<25 μm	0.921 \pm 0.002	1.906 \pm 0.002	MP-TXH-088-A
Y-74013	diogenite	<25 μm	0.924 \pm 0.003	1.925 \pm 0.003	MB-TXH-073-A
Y-74013	diogenite	25–45 μm	0.924 \pm 0.003	1.910 \pm 0.003	MB-TXH-073-B
Y-75032	diogenite	<25 μm	0.929 \pm 0.003	1.951 \pm 0.003	MB-TXH-074-A
Y-75032	diogenite	25–45 μm	0.930 \pm 0.004	1.959 \pm 0.003	MB-TXH-074-B
GRO 95555	diogenite-an	<25 μm	0.925 \pm 0.001	1.904 \pm 0.002	MP-TXH-068-A
MIL 07001	diogenite-olivine	<45 μm	0.922 \pm 0.002	1.891 \pm 0.002	MT-AWB-168-A
MIL 07001	diogenite-olivine	bulk	0.922 \pm 0.002	1.890 \pm 0.001	MT-AWB-168
Aioun el Atrouss	diogenite-pm	<25 μm	0.925 \pm 0.001	1.904 \pm 0.002	MP-TXH-081-A
Bununu	howardite	<25 μm	0.931 \pm 0.002	1.961 \pm 0.003	MP-TXH-083-A
CRE 01400	howardite	<45 μm	0.925 \pm 0.001	1.905 \pm 0.001	RM-REM-170-B
CRE 01400	howardite	<75 μm	0.925 \pm 0.002	1.909 \pm 0.002	MT-D2M-200-A
CRE 01400	howardite	<125 μm	0.933 \pm 0.012	1.925 \pm 0.008	RM-REM-170-A
EET 83376	howardite	<25 μm	0.937 \pm 0.002	1.978 \pm 0.002	MP-TXH-073-A
EET 83376	howardite	<45 μm	0.937 \pm 0.002	1.975 \pm 0.001	RM-REM-189-B
EET 83376	howardite	<75 μm	0.933 \pm 0.003	1.961 \pm 0.002	MT-D2M-242-A
EET 83376	howardite	<125 μm	0.938 \pm 0.009	1.964 \pm 0.007	RM-REM-189-A
EET 87503	howardite	<25 μm	0.930 \pm 0.003	1.967 \pm 0.003	MB-TXH-068-AP
EET 87503	howardite	<25 μm	0.932 \pm 0.003	1.977 \pm 0.004	MB-TXH-068-G

Table A1
(Continued)

Meteorite	Class	Particle Size	Centers		RELAB ID
			Band I (μm)	Band II (μm)	
EET 87503	howardite	<25 μm	0.930 ± 0.003	1.967 ± 0.003	MB-TXH-068-A
EET 87503	howardite	<45 μm	0.934 ± 0.002	1.974 ± 0.002	RM-REM-190-B
EET 87503	howardite	45–75 μm	0.931 ± 0.005	1.962 ± 0.004	MB-TXH-068-C
EET 87503	howardite	<75 μm	0.932 ± 0.004	1.969 ± 0.002	MT-D2M-243-A
EET 87503	howardite	75–125 μm	0.932 ± 0.006	1.962 ± 0.004	MB-TXH-068-D
EET 87503	howardite	<125 μm	0.934 ± 0.020	1.968 ± 0.017	RM-REM-190-A
EET 87503	howardite	125–250 μm	0.932 ± 0.006	1.963 ± 0.006	MB-TXH-068-E
EET 87503	howardite	<150 μm	0.933 ± 0.003	1.972 ± 0.004	MB-TXH-068-H
EET 87503	howardite	250–500 μm	0.935 ± 0.007	1.950 ± 0.007	MB-TXH-068-F
EET 87513	howardite	<25 μm	0.935 ± 0.003	1.979 ± 0.004	MP-TXH-074-A
EET 87513	howardite	<45 μm	0.933 ± 0.002	1.964 ± 0.002	RM-REM-192-B
EET 87513	howardite	<75 μm	0.933 ± 0.003	1.968 ± 0.003	MT-D2M-244-A
EET 87513	howardite	<125 μm	0.932 ± 0.003	1.960 ± 0.002	RM-REM-192-A
EET 87528	howardite	<45 μm	0.925 ± 0.001	1.915 ± 0.001	RM-REM-194-B
EET 87528	howardite	<125 μm	0.927 ± 0.007	1.915 ± 0.005	RM-REM-194-A
EET 87532	howardite	<75 μm	0.938 ± 0.003	1.980 ± 0.002	MT-D2M-246-A
EET 99400	howardite	<45 μm	0.936 ± 0.002	1.976 ± 0.002	RM-REM-196-B
EET 99400	howardite	<75 μm	0.935 ± 0.003	1.973 ± 0.002	MT-D2M-247-A
EET 99400	howardite	<125 μm	0.935 ± 0.011	1.961 ± 0.007	RM-REM-196-A
EET 99408	howardite	<45 μm	0.940 ± 0.001	1.980 ± 0.000	RM-REM-197-B
EET 99408	howardite	<75 μm	0.935 ± 0.003	1.975 ± 0.001	MT-D2M-204-A
EET 99408	howardite	<125 μm	0.938 ± 0.005	1.969 ± 0.003	RM-REM-197-A
Frankfort (stone)	howardite	<25 μm	0.930 ± 0.002	1.953 ± 0.003	MP-TXH-085-A
GRO 95535	howardite	<25 μm	0.932 ± 0.003	1.966 ± 0.003	MP-TXH-067-A
GRO 95535	howardite	<45 μm	0.932 ± 0.002	1.957 ± 0.002	RM-REM-183-B
GRO 95535	howardite	<75 μm	0.931 ± 0.003	1.954 ± 0.002	MT-D2M-248-A
GRO 95535	howardite	<125 μm	0.931 ± 0.005	1.964 ± 0.004	RM-REM-183-A
GRO 95574	howardite	25–125 μm	0.935 ± 0.002	1.951 ± 0.002	TB-THB-156
GRO 95574	howardite	<45 μm	0.932 ± 0.003	1.957 ± 0.002	RM-REM-184-B
GRO 95574	howardite	<75 μm	0.930 ± 0.003	1.956 ± 0.002	MT-D2M-205-A
GRO 95574	howardite	<125 μm	0.931 ± 0.005	1.950 ± 0.004	MP-TXH-125
GRO 95574	howardite	<125 μm	0.928 ± 0.007	1.938 ± 0.005	RM-REM-184-A
GRO 95581	howardite	<45 μm	0.930 ± 0.001	1.950 ± 0.001	RM-REM-185-B
GRO 95581	howardite	<75 μm	0.931 ± 0.003	1.952 ± 0.002	MT-D2M-249-A
GRO 95581	howardite	<125 μm	0.934 ± 0.006	1.967 ± 0.007	RM-REM-185-A
GRO 95602	howardite	<45 μm	0.934 ± 0.002	1.968 ± 0.002	RM-REM-186-B
GRO 95602	howardite	<75 μm	0.931 ± 0.004	1.961 ± 0.002	MT-D2M-206-A
GRO 95602	howardite	<125 μm	0.932 ± 0.010	1.945 ± 0.008	RM-REM-186-A
GRO 95633	howardite	<45 μm	0.937 ± 0.003	2.031 ± 0.158	RM-REM-187-B
GRO 95633	howardite	<125 μm	0.928 ± 0.014	1.934 ± 0.017	RM-REM-187-A
Kapoeta	howardite	<25 μm	0.931 ± 0.003	1.965 ± 0.004	MP-TXH-053-A
Kapoeta	howardite	bulk	0.931 ± 0.006	1.945 ± 0.004	MP-TXH-053
LAP 04838	howardite	<45 μm	0.938 ± 0.002	2.032 ± 0.135	RM-REM-171-B
LAP 04838	howardite	<75 μm	0.939 ± 0.003	1.981 ± 0.002	MT-D2M-250-A
LAP 04838	howardite	<75 μm	0.938 ± 0.004	1.976 ± 0.002	MT-D2M-207-A
LAP 04838	howardite	<125 μm	0.940 ± 0.004	1.982 ± 0.003	RM-REM-171-A
LAR 12326	howardite	<125 μm	0.934 ± 0.005	1.960 ± 0.001	TB-MDD-249
Le Teilleul	howardite	<25 μm	0.931 ± 0.002	1.946 ± 0.002	MP-TXH-093-A
LEW 85313	howardite	<45 μm	0.932 ± 0.003	1.963 ± 0.003	RM-REM-172-B
LEW 85313	howardite	<75 μm	0.932 ± 0.004	1.965 ± 0.001	MT-D2M-208-A
LEW 85313	howardite	<125 μm	0.930 ± 0.009	1.958 ± 0.006	RM-REM-172-A
MET 00423	howardite	<45 μm	0.938 ± 0.002	1.987 ± 0.002	RM-REM-179-B
MET 00423	howardite	<75 μm	0.934 ± 0.004	1.978 ± 0.002	MT-D2M-210-A
MET 00423	howardite	<125 μm	0.939 ± 0.012	1.979 ± 0.007	RM-REM-179-A
MET 96500	howardite	<45 μm	0.935 ± 0.001	1.977 ± 0.002	RM-REM-178-B
MET 96500	howardite	<75 μm	0.933 ± 0.003	1.967 ± 0.003	MT-D2M-252-A
MET 96500	howardite	<75 μm	0.933 ± 0.003	1.954 ± 0.002	MT-D2M-211-A
MET 96500	howardite	<125 μm	0.935 ± 0.003	1.979 ± 0.002	RM-REM-178-A
MIL 07665	howardite	<45 μm	0.927 ± 0.002	1.930 ± 0.001	RM-REM-173-B
MIL 07665	howardite	<125 μm	0.921 ± 0.004	1.882 ± 0.002	RM-REM-173-A
PCA 02009	howardite	<40 μm	0.924 ± 0.002	1.925 ± 0.001	MT-AWB-238
PCA 02013	howardite	<40 μm	0.923 ± 0.003	1.930 ± 0.002	MT-AWB-239
PCA 02013	howardite	<45 μm	0.925 ± 0.002	2.012 ± 0.113	RM-REM-174-B

Table A1
(Continued)

Meteorite	Class	Particle Size	Centers		RELAB ID
			Band I (μm)	Band II (μm)	
PCA 02013	howardite	<125 μm	0.920 \pm 0.005	1.897 \pm 0.004	RM-REM-174-A
PCA 02014	howardite	<40 μm	0.929 \pm 0.002	1.955 \pm 0.002	MT-AWB-240
PCA 02015	howardite	<40 μm	0.936 \pm 0.003	1.989 \pm 0.003	MT-AWB-241
PCA 02066	howardite	<75 μm	0.936 \pm 0.004	1.977 \pm 0.003	MT-D2M-253-A
PRA 04401	howardite	<75 μm	0.921 \pm 0.024	1.948 \pm 0.007	MT-D2M-254-A
PRA 04402	howardite	<45 μm	0.925 \pm 0.004	2.017 \pm 0.108	RM-REM-175-B
PRA 04402	howardite	<125 μm	0.920 \pm 0.008	1.933 \pm 0.018	RM-REM-175-A
QUE 94200	howardite	<25 μm	0.925 \pm 0.002	1.924 \pm 0.002	MP-TXH-069-A
QUE 94200	howardite	<45 μm	0.926 \pm 0.002	1.920 \pm 0.000	RM-REM-180-B
QUE 94200	howardite	<75 μm	0.926 \pm 0.003	1.919 \pm 0.002	MT-D2M-255-A
QUE 94200	howardite	<125 μm	0.927 \pm 0.003	1.910 \pm 0.001	RM-REM-180-A
QUE 97001	howardite	<45 μm	0.925 \pm 0.001	1.910 \pm 0.001	RM-REM-181-B
QUE 97001	howardite	<75 μm	0.925 \pm 0.003	1.915 \pm 0.001	MT-D2M-212-A
QUE 97001	howardite	<75 μm	0.926 \pm 0.003	1.920 \pm 0.001	MT-D2M-256-A
QUE 97001	howardite	<125 μm	0.928 \pm 0.004	1.903 \pm 0.003	RM-REM-181-A
QUE 97001	howardite	<125 μm	0.927 \pm 0.002	1.925 \pm 0.001	MP-TXH-126
QUE 97002	howardite	<45 μm	0.943 \pm 0.003	2.010 \pm 0.002	RM-REM-206-B
QUE 97002	howardite	<75 μm	0.938 \pm 0.005	1.998 \pm 0.003	MT-D2M-213-A
QUE 97002	howardite	<75 μm	0.941 \pm 0.004	1.996 \pm 0.002	MT-D2M-257-A
QUE 97002	howardite	<125 μm	0.948 \pm 0.006	1.997 \pm 0.006	RM-REM-206-A
QUE 99033	howardite	<45 μm	0.928 \pm 0.002	1.924 \pm 0.002	RM-REM-218-B
QUE 99033	howardite	<75 μm	0.926 \pm 0.003	1.917 \pm 0.002	MT-D2M-214-A
QUE 99033	howardite	<125 μm	0.930 \pm 0.001	1.915 \pm 0.001	RM-REM-218-A
QUE 99058	howardite	<45 μm	0.926 \pm 0.002	1.991 \pm 0.108	RM-REM-182-B
QUE 99058	howardite	<125 μm	0.929 \pm 0.008	1.912 \pm 0.005	RM-REM-182-A
SAN 03472	howardite	<45 μm	0.929 \pm 0.002	1.954 \pm 0.002	RM-REM-176-B
SAN 03472	howardite	<75 μm	0.931 \pm 0.003	1.955 \pm 0.001	MT-D2M-258-A
SAN 03472	howardite	<125 μm	0.931 \pm 0.006	1.938 \pm 0.008	RM-REM-176-A
Sarıçiçek	howardite	<25 μm	0.932 \pm 0.002	1.966 \pm 0.002	MT-PMJ-311-A
Sarıçiçek	howardite	<125 μm	0.933 \pm 0.003	1.963 \pm 0.002	MT-PMJ-311-C
Sarıçiçek	howardite	125–500 μm	0.934 \pm 0.004	1.958 \pm 0.003	MT-PMJ-311-B
SCO 06040	howardite	<45 μm	0.934 \pm 0.003	1.982 \pm 0.003	RM-REM-177-B
SCO 06040	howardite	<75 μm	0.932 \pm 0.005	1.974 \pm 0.003	MT-D2M-215-A
SCO 06040	howardite	<125 μm	0.932 \pm 0.007	1.975 \pm 0.002	RM-REM-177-A
Y-7308	howardite	<25 μm	0.929 \pm 0.002	1.942 \pm 0.003	MP-TXH-097-A
Y-790727	howardite	<25 μm	0.935 \pm 0.002	1.965 \pm 0.002	MP-TXH-098-A
Y-791573	howardite	<25 μm	0.929 \pm 0.002	1.951 \pm 0.002	MP-TXH-099-A
A-881819	euclite	<25 μm	0.933 \pm 0.003	1.977 \pm 0.003	MP-TXH-096-A
MIL 11290	euclite	<125 μm	0.959 \pm 0.005	2.020 \pm 0.002	TB-MDD-270
Y-793591	euclite	<25 μm	0.942 \pm 0.003	2.027 \pm 0.003	MT-TXH-043-A
DOM 08001	euclite-br	<125 μm	0.951 \pm 0.003	2.009 \pm 0.003	TB-MDD-220
EET 87542	euclite-br	<25 μm	0.941 \pm 0.004	2.012 \pm 0.005	MP-TXH-075-A
EET 87542	euclite-br	<45 μm	0.942 \pm 0.003	1.995 \pm 0.002	RM-REM-207-B
EET 87542	euclite-br	<125 μm	0.948 \pm 0.005	1.991 \pm 0.003	RM-REM-207-A
EET 87542	euclite-br	bulk	0.950 \pm 0.005	1.984 \pm 0.007	TB-RPB-014
EET 92003	euclite-br	<125 μm	0.936 \pm 0.002	2.002 \pm 0.002	MP-TXH-118
GRA 98037	euclite-br	<45 μm	0.949 \pm 0.002	2.023 \pm 0.002	RM-REM-208-B
GRA 98037	euclite-br	<125 μm	0.946 \pm 0.006	2.017 \pm 0.005	RM-REM-208-A
GRO 06059	euclite-br	<45 μm	0.950 \pm 0.001	2.030 \pm 0.000	RM-REM-209-B
GRO 06059	euclite-br	<125 μm	0.945 \pm 0.006	2.002 \pm 0.005	RM-REM-209-A
GRO 95533	euclite-br	<25 μm	0.943 \pm 0.003	2.011 \pm 0.002	MP-TXH-066-A
HOW 88401	euclite-br	<125 μm	0.947 \pm 0.005	1.990 \pm 0.000	TB-MDD-238
MIL 07004	euclite-br	<125 μm	0.947 \pm 0.005	2.007 \pm 0.005	TB-MDD-266
PCA 91006	euclite-br	<125 μm	0.943 \pm 0.002	2.000 \pm 0.002	MP-TXH-119
PCA 91007	euclite-br	<125 μm	0.949 \pm 0.004	2.025 \pm 0.003	MP-TXH-120
PCA 91007	euclite-br	bulk	0.951 \pm 0.006	1.996 \pm 0.007	TB-RPB-016
PCA 91179	euclite-br	<45 μm	0.944 \pm 0.002	1.999 \pm 0.002	RM-REM-212-B
PCA 91179	euclite-br	<125 μm	0.944 \pm 0.004	2.001 \pm 0.003	RM-REM-212-A
SCO 06041	euclite-br	<45 μm	0.937 \pm 0.002	1.999 \pm 0.002	RM-REM-210-B
SCO 06041	euclite-br	<125 μm	0.938 \pm 0.010	1.978 \pm 0.008	RM-REM-210-A
TIL 82403	euclite-br	<45 μm	0.945 \pm 0.001	1.995 \pm 0.001	RM-REM-211-B
TIL 82403	euclite-br	<125 μm	0.948 \pm 0.006	1.972 \pm 0.004	RM-REM-211-A
Binda	euclite-cm	<25 μm	0.930 \pm 0.002	1.934 \pm 0.002	MP-TXH-082-A

Table A1
(Continued)

Meteorite	Class	Particle Size	Centers		RELAB ID
			Band I (μm)	Band II (μm)	
Moore County	eucreite-cm	<25 μm	0.940 \pm 0.002	1.990 \pm 0.002	MP-TXH-086-A
Serra de Magé	eucreite-cm	<25 μm	0.932 \pm 0.003	1.973 \pm 0.002	MP-TXH-092-A
Y-980318	eucreite-cm	<75 μm	0.940 \pm 0.000	1.990 \pm 0.000	MT-CMP-061
ALH 85001	eucreite-Mg-rich	<25 μm	0.928 \pm 0.002	1.950 \pm 0.002	MB-TXH-099-D
ALH 85001	eucreite-Mg-rich	<25 μm	0.928 \pm 0.003	1.958 \pm 0.003	MB-TXH-099-W
ALH 85001	eucreite-Mg-rich	<45 μm	0.929 \pm 0.002	1.947 \pm 0.002	RM-REM-203-B
ALH 85001	eucreite-Mg-rich	<125 μm	0.929 \pm 0.002	1.949 \pm 0.002	RM-REM-203-A
ALH 85001	eucreite-Mg-rich	bulk	0.927 \pm 0.012	1.922 \pm 0.006	TB-RPB-015
EET 87520	eucreite-Mg-rich	<45 μm	0.955 \pm 0.001	2.004 \pm 0.002	MT-HYM-029
EET 87548	eucreite-Mg-rich	<125 μm	0.938 \pm 0.004	1.960 \pm 0.000	TB-MDD-233
Y-980433	eucreite-Mg-rich	<63 μm	0.940 \pm 0.002	1.974 \pm 0.002	MT-CMP-065
A-87272	eucreite-mmict	<25 μm	0.943 \pm 0.003	2.018 \pm 0.002	MP-TXH-094-A
Béréba	eucreite-mmict	<25 μm	0.944 \pm 0.003	2.031 \pm 0.002	MP-TXH-089-A
Bouvante	eucreite-mmict	<25 μm	0.949 \pm 0.003	2.022 \pm 0.002	MP-TXH-090-A
Bouvante	eucreite-mmict	<44 μm	0.956 \pm 0.005	1.986 \pm 0.007	TB-TJM-118
Bouvante	eucreite-mmict	<250 μm	0.956 \pm 0.005	1.990 \pm 0.000	TB-RPB-028
Bouvante	eucreite-mmict	<500 μm	0.951 \pm 0.005	1.991 \pm 0.003	TB-RPB-029
Cachari	eucreite-mmict	<25 μm	0.944 \pm 0.002	2.010 \pm 0.001	MP-TXH-084-A
Chervony Kut	eucreite-mmict	<38 μm	0.944 \pm 0.002	1.991 \pm 0.002	MT-HYM-035
Ibitira	eucreite-mmict	<25 μm	0.941 \pm 0.002	1.994 \pm 0.002	MP-TXH-054-A
Jonzac	eucreite-mmict	<25 μm	0.942 \pm 0.002	2.009 \pm 0.002	MP-TXH-091-A
Juvinas	eucreite-mmict	<25 μm	0.939 \pm 0.002	1.995 \pm 0.002	MB-TXH-070-A
Juvinas	eucreite-mmict	25–45 μm	0.947 \pm 0.003	1.988 \pm 0.002	MB-TXH-070-B
Juvinas	eucreite-mmict	45–75 μm	0.955 \pm 0.004	1.980 \pm 0.002	MB-TXH-070-C
Juvinas	eucreite-mmict	75–125 μm	0.960 \pm 0.005	1.973 \pm 0.003	MB-TXH-070-D
Juvinas	eucreite-mmict	125–250 μm	0.961 \pm 0.006	1.969 \pm 0.004	MB-TXH-070-E
Juvinas	eucreite-mmict	<250 μm	0.958 \pm 0.004	1.951 \pm 0.003	TB-RPB-153
Millbillillie	eucreite-mmict	<25 μm	0.939 \pm 0.002	2.015 \pm 0.003	MB-TXH-069-A
Millbillillie	eucreite-mmict	25–45 μm	0.941 \pm 0.003	2.010 \pm 0.002	MB-TXH-069-B
Millbillillie	eucreite-mmict	45–75 μm	0.943 \pm 0.004	2.005 \pm 0.003	MB-TXH-069-C
Millbillillie	eucreite-mmict	<75 μm	0.947 \pm 0.003	2.005 \pm 0.002	MS-JTW-048-A
Millbillillie	eucreite-mmict	75–125 μm	0.944 \pm 0.004	2.004 \pm 0.003	MB-TXH-069-D
Millbillillie	eucreite-mmict	<80 μm	0.940 \pm 0.003	2.020 \pm 0.003	HH-CMP-003
Padvarninkai	eucreite-mmict	<25 μm	0.941 \pm 0.003	2.008 \pm 0.003	MB-TXH-096-C
Padvarninkai	eucreite-mmict	25–45 μm	0.947 \pm 0.003	2.001 \pm 0.002	MB-TXH-096-D
Stannern	eucreite-mmict	<25 μm	0.941 \pm 0.003	2.026 \pm 0.003	MB-TXH-097-A
Stannern	eucreite-mmict	25–45 μm	0.947 \pm 0.004	2.015 \pm 0.002	MB-TXH-097-B
Y-792510	eucreite-mmict	<25 μm	0.944 \pm 0.002	2.029 \pm 0.002	MT-TXH-041-A
Y-792510	eucreite-mmict	bulk	0.944 \pm 0.006	1.981 \pm 0.007	TB-RPB-007
ALHA76005	eucreite-pmict	<25 μm	0.938 \pm 0.003	1.985 \pm 0.002	MB-TXH-066-A
ALHA76005	eucreite-pmict	<25 μm	0.938 \pm 0.002	1.997 \pm 0.002	MB-TXH-066-G
ALHA76005	eucreite-pmict	25–45 μm	0.942 \pm 0.003	1.990 \pm 0.002	MB-TXH-066-B
ALHA76005	eucreite-pmict	25–125 μm	0.940 \pm 0.001	1.990 \pm 0.000	TB-THB-155
ALHA76005	eucreite-pmict	<45 μm	0.940 \pm 0.001	2.000 \pm 0.001	RM-REM-198-B
ALHA76005	eucreite-pmict	45–75 μm	0.946 \pm 0.004	1.983 \pm 0.003	MB-TXH-066-C
ALHA76005	eucreite-pmict	75–125 μm	0.948 \pm 0.005	1.986 \pm 0.003	MB-TXH-066-D
ALHA76005	eucreite-pmict	<125 μm	0.944 \pm 0.005	2.012 \pm 0.003	RM-REM-198-A
ALHA76005	eucreite-pmict	125–250 μm	0.945 \pm 0.006	1.974 \pm 0.003	MB-TXH-066-E
ALHA76005	eucreite-pmict	<150 μm	0.939 \pm 0.002	1.992 \pm 0.002	MB-TXH-066-H
ALHA76005	eucreite-pmict	<250 μm	0.946 \pm 0.005	1.982 \pm 0.004	TB-RPB-024
ALHA76005	eucreite-pmict	250–500 μm	0.945 \pm 0.006	1.969 \pm 0.004	MB-TXH-066-F
ALHA76005	eucreite-pmict	bulk	0.944 \pm 0.008	1.974 \pm 0.006	TB-RPB-023
ALHA77302	eucreite-pmict	<45 μm	0.938 \pm 0.002	1.976 \pm 0.002	RM-REM-199-B
ALHA77302	eucreite-pmict	<125 μm	0.941 \pm 0.007	2.006 \pm 0.005	RM-REM-199-A
ALHA78040	eucreite-pmict	<45 μm	0.939 \pm 0.002	1.986 \pm 0.002	RM-REM-213-B
ALHA78040	eucreite-pmict	<125 μm	0.942 \pm 0.008	1.994 \pm 0.006	RM-REM-213-A
ALHA78132	eucreite-pmict	<25 μm	0.934 \pm 0.002	1.968 \pm 0.003	MB-TXH-072-A
ALHA78132	eucreite-pmict	25–45 μm	0.938 \pm 0.003	1.973 \pm 0.003	MB-TXH-072-B
ALHA78132	eucreite-pmict	<45 μm	0.938 \pm 0.002	1.983 \pm 0.002	RM-REM-200-B
ALHA78132	eucreite-pmict	45–75 μm	0.941 \pm 0.004	1.969 \pm 0.003	MB-TXH-072-C
ALHA78132	eucreite-pmict	<125 μm	0.943 \pm 0.008	1.966 \pm 0.003	RM-REM-200-A
ALHA79017	eucreite-pmict	<45 μm	0.938 \pm 0.002	1.995 \pm 0.001	RM-REM-214-B
ALHA79017	eucreite-pmict	<125 μm	0.943 \pm 0.026	2.009 \pm 0.015	RM-REM-214-A

Table A1
(Continued)

Meteorite	Class	Particle Size	Centers		RELAB ID
			Band I (μm)	Band II (μm)	
ALHA80102	euclite-pmict	<45 μm	0.936 \pm 0.002	1.975 \pm 0.001	RM-REM-215-B
ALHA80102	euclite-pmict	<125 μm	0.937 \pm 0.024	1.990 \pm 0.016	RM-REM-215-A
ALHA81006	euclite-pmict	<45 μm	0.938 \pm 0.002	1.985 \pm 0.001	RM-REM-201-B
ALHA81006	euclite-pmict	<125 μm	0.943 \pm 0.018	1.987 \pm 0.014	RM-REM-201-A
ALHA81010	euclite-pmict	<45 μm	0.941 \pm 0.002	1.996 \pm 0.002	RM-REM-216-B
ALHA81010	euclite-pmict	<125 μm	0.942 \pm 0.020	1.989 \pm 0.012	RM-REM-216-A
ALHA81011	euclite-pmict	<125 μm	0.953 \pm 0.003	2.056 \pm 0.005	MP-TXH-122
ALHA81011	euclite-pmict	bulk	0.960 \pm 0.014	2.063 \pm 0.008	TB-RPB-013
EETA79005	euclite-pmict	<25 μm	0.937 \pm 0.002	1.971 \pm 0.002	MP-TXH-072-A
EETA79005	euclite-pmict	<45 μm	0.937 \pm 0.002	1.975 \pm 0.001	RM-REM-204-B
EETA79005	euclite-pmict	<125 μm	0.939 \pm 0.008	1.971 \pm 0.005	RM-REM-204-A
EETA79005	euclite-pmict	<250 μm	0.939 \pm 0.003	1.965 \pm 0.005	TB-RPB-026
EETA79005	euclite-pmict	bulk	0.939 \pm 0.005	1.951 \pm 0.013	TB-RPB-025
EETA79006	euclite-pmict	<125 μm	0.938 \pm 0.002	1.981 \pm 0.003	MP-TXH-123
EET 83228	euclite-pmict	<125 μm	0.940 \pm 0.002	1.980 \pm 0.000	TB-MDD-231
EET 87509	euclite-pmict	<45 μm	0.938 \pm 0.002	1.980 \pm 0.001	RM-REM-191-B
EET 87509	euclite-pmict	<75 μm	0.934 \pm 0.003	1.975 \pm 0.001	MT-D2M-201-A
EET 87509	euclite-pmict	<125 μm	0.940 \pm 0.011	1.970 \pm 0.008	RM-REM-191-A
EET 87518	euclite-pmict	<45 μm	0.936 \pm 0.002	1.975 \pm 0.001	RM-REM-193-B
EET 87518	euclite-pmict	<75 μm	0.938 \pm 0.003	1.979 \pm 0.002	MT-D2M-245-A
EET 87518	euclite-pmict	<125 μm	0.938 \pm 0.003	1.974 \pm 0.002	RM-REM-193-A
EET 87531	euclite-pmict	<45 μm	0.933 \pm 0.002	1.959 \pm 0.002	RM-REM-195-B
EET 87531	euclite-pmict	<125 μm	0.932 \pm 0.009	1.934 \pm 0.007	RM-REM-195-A
EET 90020	euclite-pmict	bulk	0.947 \pm 0.007	1.982 \pm 0.005	TB-RPB-020
LEW 85303	euclite-pmict	<25 μm	0.947 \pm 0.003	2.037 \pm 0.003	MP-TXH-078-A
LEW 86001	euclite-pmict	<75 μm	0.948 \pm 0.003	2.014 \pm 0.002	MT-D2M-251-A
LEW 87004	euclite-pmict	<25 μm	0.937 \pm 0.003	1.985 \pm 0.002	MP-TXH-079-A
LEW 87004	euclite-pmict	<45 μm	0.936 \pm 0.002	1.984 \pm 0.002	RM-REM-205-B
LEW 87004	euclite-pmict	<75 μm	0.936 \pm 0.003	1.985 \pm 0.001	MT-D2M-209-A
LEW 87004	euclite-pmict	<125 μm	0.939 \pm 0.006	1.988 \pm 0.005	RM-REM-205-A
LEW 87004	euclite-pmict	bulk	0.939 \pm 0.004	1.981 \pm 0.003	TB-RPB-019
Macibini Clast 3	euclite-pmict	<63 μm	0.943 \pm 0.005	2.008 \pm 0.004	TB-RPB-027
Pasamonte	euclite-pmict	<25 μm	0.942 \pm 0.003	2.020 \pm 0.002	MP-TXH-087-A
Petersburg	euclite-pmict	<25 μm	0.937 \pm 0.003	1.982 \pm 0.003	MP-TXH-070-A
Y-74450	euclite-pmict	<25 μm	0.936 \pm 0.003	2.007 \pm 0.003	MB-TXH-071-A
Y-74450	euclite-pmict	25–45 μm	0.938 \pm 0.004	1.992 \pm 0.003	MB-TXH-071-B
Y-74450	euclite-pmict	45–75 μm	0.939 \pm 0.004	1.992 \pm 0.003	MB-TXH-071-C
Y-74450	euclite-pmict	75–125 μm	0.940 \pm 0.005	1.992 \pm 0.004	MB-TXH-071-D
Y-75011	euclite-pmict	bulk	0.945 \pm 0.011	2.001 \pm 0.013	TB-RPB-008
Y-792769	euclite-pmict	<25 μm	0.943 \pm 0.003	2.026 \pm 0.003	MT-TXH-042-A
Y-82082	euclite-pmict	<25 μm	0.948 \pm 0.003	2.035 \pm 0.003	MT-TXH-044-A
ALHA81001	euclite-unbr	<45 μm	0.940 \pm 0.002	2.012 \pm 0.003	MT-HYM-030
ALHA81001	euclite-unbr	<125 μm	0.939 \pm 0.002	2.043 \pm 0.005	MP-TXH-121
BTN 00300	euclite-unbr	<45 μm	0.938 \pm 0.005	1.996 \pm 0.002	MT-HYM-032
EET 83251	euclite-unbr	bulk	0.938 \pm 0.006	1.960 \pm 0.013	TB-RPB-022
EET 90020	euclite-unbr	<25 μm	0.941 \pm 0.002	2.011 \pm 0.002	MP-TXH-076-A
EET 90020	euclite-unbr	bulk	0.947 \pm 0.007	1.982 \pm 0.005	TB-RPB-020
GRA 98098	euclite-unbr	<38 μm	0.941 \pm 0.002	2.004 \pm 0.002	MT-HYM-034
MAC 02522	euclite-unbr	<45 μm	0.974 \pm 0.002	2.115 \pm 0.002	MT-HYM-028
MET 01081	euclite-unbr	<45 μm	0.943 \pm 0.005	1.989 \pm 0.002	MT-HYM-033
PCA 82501	euclite-unbr	<125 μm	0.945 \pm 0.005	2.002 \pm 0.006	MP-TXH-124
PCA 82501	euclite-unbr	bulk	0.946 \pm 0.009	1.992 \pm 0.010	TB-RPB-012
PCA 82502	euclite-unbr	<25 μm	0.945 \pm 0.002	2.027 \pm 0.002	MP-TXH-080-A
PCA 82502	euclite-unbr	bulk	0.950 \pm 0.002	2.010 \pm 0.000	TB-RPB-021
PCA 91078	euclite-unbr	<45 μm	0.968 \pm 0.011	1.996 \pm 0.002	MT-HYM-031

(This table is available in machine-readable form.)

Appendix B

Bulk Pyroxene Compositions of the HEDs

We estimate the bulk pyroxene compositions (Table B1) for a number of HEDs in our study. We list the meteorite name, its specific classification, the particle size, its estimated bulk Fs (mol%) and Wo (mol%) contents, and a reference for the pyroxene mineralogy. We group the

meteorites by both type and subtype. We use the abbreviation *diogenite-an* for an anomalous diogenite, *diogenite-olivine* for an olivine diogenite, *euclite-br* for a brecciated euclite, *euclite-cm* for a cumulate euclite, *euclite-Mg-rich* for a Mg-rich euclite, *euclite-mmict* for a monomict euclite, *euclite-pmict* for a polymict euclite, and *euclite-unbr* for an unbrecciated euclite.

Table B1
Bulk Pyroxene Compositions of HEDs

Meteorite	Type	Bulk Fs (mol%)	Bulk Wo (mol%)	Reference
A-881526	diogenite	22.6	2.6	Kojima & Yamaguchi (2005)
ALHA77256	diogenite	23	2	Mason (1981)
ALH 85015	diogenite	25	2.05	Score & Mason (1986b)
EETA79002	diogenite	22	2	Score & Reid (1980)
EET 83246	diogenite	26	3	Berkley & Boynton (1992)
Ellemeet	diogenite	22.8	1.54	Buchanan (unpublished)
GRA 98108	diogenite	22	2	McBride & McCoy (2000)
Johnstown	diogenite	23.5	2.8	Zema et al. (1997, 1999)
LAP 02216	diogenite	23	2	McBride et al. (2003a)
LAP 03630	diogenite	24.4	2.3	Table 2
LAP 03979	diogenite	25	3	McBride et al. (2004)
LAP 91900	diogenite	23	2	Satterwhite & Mason (1992)
LEW 88008	diogenite	30	4	Marlow & Mason (1990)
MET 00436	diogenite	26	1.5	McBride et al. (2001b)
MET 01084	diogenite	26	2	McBride & McCoy (2003)
MIL 03368	diogenite	27	3	McBride et al. (2005)
PCA 02008	diogenite	24	2.5	Beck & McSween (2010)
QUE 99050	diogenite	21	2	McBride et al. (2001a)
Tatahouine	diogenite	23	1.5	Burbine et al. (2009)
Y-74013	diogenite	26.5	3	Takeda et al. (1981)
GRO 95555	diogenite-an	24	2	Schwarz et al. (1996)
MIL 07001	diogenite-olivine	23	2	Harrington et al. (2008)
Aioun el Atrouss	diogenite-pm	25.1	3.7	Basaltic Volcanism Study Project (1981)
EET 87503	howardite	40.3	8.1	Burbine et al. (2009)
EET 87513	howardite	39.4	8.48	Buchanan (1995)
EET 87528	howardite	23.8	2.55	Buchanan et al. (2000a)
GRO 95574	howardite	32.2	6.1	Table 2
LEW 85313	howardite	33	8	Score & Mason (1988a)
EET 87542	euclite-br	44	13	Burbine et al. (2001)
EET 92003	euclite-br	49	13	Satterwhite & Mason (1993b)
GRO 95533	euclite-br	61.5	4	Score & Mason (1996)
PCA 91007	euclite-br	55	11	Burbine et al. (2001)
PCA 91179	euclite-br	55	4	Satterwhite & Mason (1993a)
Binda	euclite-cm	30	6	Basaltic Volcanism Study Project (1981)
Moore County	euclite-cm	44	10	Basaltic Volcanism Study Project (1981)
Serra de Magé	euclite-cm	39	10	Harlow et al. (1979)
Y-980318	euclite-cm	41	12	Buchanan (unpublished)
ALH 85001	euclite-Mg-rich	32	2	Score & Mason (1986a)
EET 87520	euclite-Mg-rich	50	5	Score & Mason (1988b)
EET 87548	euclite-Mg-rich	38	11	Satterwhite & Mason (1989)
Y-980433	euclite-Mg-rich	41	12	Buchanan (unpublished)
Bouvante	euclite-mmict	53.5	14	Burbine et al. (2009)
Cachari	euclite-mmict	60	2	Abdu et al. (2007)
Ibitira	euclite-mmict	48	15	Steele & Smith (1976)
Juvinas	euclite-mmict	51.8	11.3	Basaltic Volcanism Study Project (1981)
Padvarninkai	euclite-mmict	55	9	Yamaguchi et al. (1993)
Stannern	euclite-mmict	55.8	9.6	Basaltic Volcanism Study Project (1981)
ALHA76005	euclite-pmict	48.8	13.8	Table 2
EETA79005	euclite-pmict	43.2	10.3	Burbine et al. (2001)
EET 87509	euclite-pmict	44.3	12.3	Buchanan (1995)
EET 87518	euclite-pmict	38.7	6.6	Buchanan et al. (2000a)
EET 87531	euclite-pmict	43.9	7.5	Buchanan (1995)

Table B1
(Continued)

Meteorite	Type	Bulk Fs (mol%)	Bulk Wo (mol%)	Reference
LEW 87004	eucrite-pmict	45	11	Burbine et al. (2001)
Macibini Clast 3	eucrite-pmict	57.2	7.97	Buchanan et al. (2000b)
Pasamonte	eucrite-pmict	43.5	13.7	Basaltic Volcanism Study Project (1981)
Petersburg	eucrite-pmict	40.6	9.4	Buchanan (1995)
ALHA81001	eucrite-unbr	59	1.6	Score & Mason (1983)
EET 83251	eucrite-unbr	46	12	Burbine et al. (2001)
EET 90020	eucrite-unbr	53	13	Burbine et al. (2001)
PCA 82501	eucrite-unbr	54	9	Burbine et al. (2001)
PCA 82502	eucrite-unbr	53	14	Burbine et al. (2001)

Appendix C**V-type Observations Used in this Study**

We list in Table C1 each V-type asteroid spectrum that was analyzed, the near-infrared observation date,

distance from Earth at time of the near-infrared observation (r) (au), the estimated surface temperature (T) (K) at that distance from the Sun, and the reference for each spectrum.

Table C1
Observational Circumstances of V-types

Asteroid	Near-Infrared Observation Date (UT)	r (au)	T (K)	Reference
(4) Vesta	2000 Oct 09	2.262	180	Moskovitz et al. (2010)
(4) Vesta	2001 Sep 29	2.555	169	Reddy & Sanchez (2016)
(4) Vesta	2009 Nov 18	2.477	174	SMASS (2023)
(809) Lundia	2008 Aug 12	1.956	196	Reddy & Sanchez (2016)
(809) Lundia	2008 Aug 26	1.933	197	Moskovitz et al. (2010)
(956) Elisa	2008 Jul 05	1.849	202	Moskovitz et al. (2010)
(956) Elisa	2008 Oct 09	1.850	202	Moskovitz et al. (2010)
(1459) Magnya	2002 Mar 23	3.846	140	Hardersen et al. (2004)
(1468) Zomba	2009 Apr 26	2.512	173	Moskovitz et al. (2010)
(1929) Kollaa	2001 Feb 19	2.210	185	DeMeo et al. (2009)
(2011) Veteraniya	2003 Aug 14	2.035	192	Reddy & Sanchez (2016)
(2011) Veteraniya	2014 Aug 26	2.042	192	Hardersen et al. (2015)
(2045) Peking	2002 Jan 14	2.484	174	DeMeo et al. (2009)
(2045) Peking	2003 Feb 17	2.267	182	Reddy & Sanchez (2016)
(2045) Peking	2008 Aug 26	2.499	174	Moskovitz et al. (2010)
(2168) Swope	2015 Jan 16	2.826	163	Hardersen et al. (2018)
(2168) Swope	2015 Jan 17	2.825	163	Hardersen et al. (2018)
(2168) Swope	2015 Jan 19	2.825	163	Hardersen et al. (2018)
(2371) Dimitrov	2009 Aug 01	2.474	174	Moskovitz et al. (2010)
(2442) Corbett	2002 Sep 15	2.251	183	DeMeo et al. (2009)
(2511) Patterson	2004 May 07	2.233	184	Moskovitz et al. (2010)
(2566) Kirghizia	2002 May 08	2.409	177	DeMeo et al. (2009)
(2653) Principia	2002 Nov 26	2.530	172	Moskovitz et al. (2010)
(2653) Principia	2005 Jul 16	2.593	170	Moskovitz et al. (2010)
(2763) Jeans	2004 Jun 26	2.236	183	Moskovitz et al. (2010)
(2763) Jeans	2008 Jul 05	1.992	194	Moskovitz et al. (2010)
(2763) Jeans	2008 Aug 26	1.916	198	Moskovitz et al. (2010)
(2795) Lepage	2005 Apr 09	2.257	183	Moskovitz et al. (2010)
(2851) Harbin	2001 Aug 24	2.418	176	DeMeo et al. (2009)
(2851) Harbin	2003 Jan 12	2.338	179	Moskovitz et al. (2010)
(2912) Lapalma	2001 Feb 20	2.141	188	DeMeo et al. (2009)
(3155) Lee	2001 Jun 22	2.557	172	DeMeo et al. (2009)
(3155) Lee	2005 Jul 14	2.427	176	Moskovitz et al. (2010)
(3715) Štohl	2015 Jan 15	2.318	180	Hardersen et al. (2018)
(3715) Štohl	2015 Jan 19	2.323	180	Hardersen et al. (2018)

Table C1
(Continued)

Asteroid	Near-Infrared Observation Date (UT)	r (au)	T (K)	Reference
(3782) Celle	2002 Nov 26	2.602	170	Moskovitz et al. (2010)
(3782) Celle	2004 Jun 25	2.191	185	Moskovitz et al. (2010)
(3782) Celle	2015 Jan 15	2.310	181	Hardersen et al. (2018)
(3782) Celle	2015 Jan 16	2.309	181	Hardersen et al. (2018)
(3849) Incidentia	2015 Jan 16	2.400	177	Hardersen et al. (2018)
(3849) Incidentia	2015 Jan 17	2.401	177	Hardersen et al. (2018)
(3867) Shiretoko	2013 Jan 14	2.151	187	Hardersen et al. (2014)
(4038) Kristina	2002 Oct 28	2.080	190	DeMeo et al. (2009)
(4188) Kitezh	2002 Aug 14	2.102	189	DeMeo et al. (2009)
(5111) Jacliff	2005 Sep 05	2.057	191	Moskovitz et al. (2010)
(5235) Jean-Loup	2013 Jan 14	2.590	170	Hardersen et al. (2014)
(5560) Amytis	2013 Jan 14	2.507	173	Hardersen et al. (2014)
(5754) 1992 FR ₂	2015 Jan 15	2.434	176	Hardersen et al. (2018)
(5754) 1992 FR ₂	2015 Jan 19	2.439	176	Hardersen et al. (2018)
(5875) Kuga	2014 Sep 03	2.391	177	Hardersen et al. (2015)
(6331) 1992 FZ ₁	2013 Jan 14	2.635	169	Hardersen et al. (2014)
(6976) Kanatsu	2013 Jan 14	2.444	176	Hardersen et al. (2014)
(7800) Zhongkeyuan	2009 Jan 09	2.512	173	Moskovitz et al. (2010)
(8149) Ruff	2014 Sep 03	2.355	179	Hardersen et al. (2015)
(9147) Kourakuen	2014 Aug 26	2.077	190	Hardersen et al. (2015)
(9553) Colas	2014 Sep 03	2.107	189	Hardersen et al. (2015)
(10537) 1991 RY ₁₆	2008 Jan 30	2.844	163	Moskovitz et al. (2010)
(10666) Feldberg	2015 Jan 16	2.094	190	Hardersen et al. (2018)
(10666) Feldberg	2015 Jan 19	2.094	190	Hardersen et al. (2018)
(15237) 1988 RL ₆	2014 Sep 03	2.050	192	Hardersen et al. (2015)
(15237) 1988 RL ₆	2014 Sep 04	2.051	192	Hardersen et al. (2015)
(17469) 1991 BT	2013 Jan 14	2.233	184	Hardersen et al. (2014)
(19165) Nariyuki	2015 Jan 19	2.121	188	Hardersen et al. (2018)
(26886) 1994 TJ ₂	2008 Jul 05	2.088	190	Moskovitz et al. (2010)
(27343) Deannashea	2008 Aug 26	1.938	197	Moskovitz et al. (2010)
(29796) 1999 CW ₇₇	2013 Jan 14	2.215	184	Hardersen et al. (2014)
(30872) 1992 EM ₁₇	2013 Jan 14	2.343	179	Hardersen et al. (2014)
(31414) Rotarysusa	2014 Sep 03	1.957	196	Hardersen et al. (2015)
(32940) 1995 UW ₄	2014 Sep 04	1.895	199	Hardersen et al. (2015)
(33881) 2000 JK ₆₆	2007 Nov 23	1.767	206	Moskovitz et al. (2010)
(38070) Redwine	2006 Oct 05	1.902	199	Moskovitz et al. (2010)

Appendix D V-type Properties

We list in Table D1 each V-type asteroid that had its spectrum or spectra analyzed, its semimajor axis (a) (au), if it is a member of the Vesta family, if it is a Mars crosser, its diameter (km), and its visual geometric albedo. Diameters and visual geometric albedos are from NEOWISE (Mainzer et al. 2016) except for

Vesta and Magnya. Vesta's diameter is an average of its three axes from Dawn observations (Russell et al. 2012), and its albedo is from IRAS (Infrared Astronomical Satellite) (Tedesco et al. 2004). Magnya's albedo and diameter are from Delbo et al. (2006). For objects with multiple NEOWISE diameters and albedos, we list the diameters that have the lowest uncertainties and the albedo associated with that diameter.

Table D1
Physical and Orbital Properties of V-types

Asteroid	a (au)	Vesta Family	Mars Crosser	Diameter (km)	Visual Geometric Albedo
(4) Vesta	2.362	yes		525.4 ± 0.2	0.423 ± 0.053
(809) Lundia	2.283			9.450 ± 0.184	0.379 ± 0.084
(956) Elisa	2.298			10.474 ± 0.208	0.147 ± 0.022
(1459) Magnya	3.150			17 ± 1	0.37 ± 0.06
(1468) Zomba	2.182		yes
(1929) Kollaa	2.363	yes		7.772 ± 0.147	0.385 ± 0.096
(2011) Veteraniya	2.387			5.193 ± 0.646	0.463 ± 0.100
(2045) Peking	2.380	yes		9.664 ± 0.098	0.249 ± 0.045

Table D1
(Continued)

Asteroid	a (au)	Vesta Family	Mars Crosser	Diameter (km)	Visual Geometric Albedo
(2168) Swope	2.452			8.205 ± 0.058	0.263 ± 0.011
(2371) Dimitrov	2.440			7.465 ± 0.354	0.348 ± 0.050
(2442) Corbett	2.388			8.327 ± 0.384	0.255 ± 0.043
(2511) Patterson	2.299	yes		7.849 ± 0.174	0.287 ± 0.039
(2566) Kirghizia	2.450			7.816 ± 0.172	0.264 ± 0.029
(2653) Principia	2.444			9.822 ± 0.984	0.256 ± 0.091
(2763) Jeans	2.404			7.514 ± 0.157	0.412 ± 0.079
(2795) Lepage	2.296	yes		5.882 ± 0.361	0.353 ± 0.027
(2851) Harbin	2.478			8.838 ± 0.236	0.358 ± 0.026
(2912) Lapalma	2.289			6.519 ± 0.289	0.456 ± 0.052
(3155) Lee	2.343	yes	
(3715) Štohl	2.315			4.913 ± 0.065	0.384 ± 0.068
(3782) Celle	2.415			5.924 ± 0.230	0.503 ± 0.078
(3849) Incidentia	2.474			5.798 ± 0.125	0.398 ± 0.041
(3867) Shiretoko	2.351			5.345 ± 0.153	0.324 ± 0.058
(4038) Kristina	2.366	yes	
(4188) Kitezh	2.335			6.588 ± 0.156	0.338 ± 0.038
(5111) Jacliff	2.354	yes		6.447 ± 0.129	0.425 ± 0.039
(5235) Jean-Loup	2.297			6.709 ± 0.109	0.360 ± 0.056
(5560) Amytis	2.286		
(5754) 1992 FR ₂	2.267			6.337 ± 0.078	0.277 ± 0.031
(5875) Kuga	2.379			7.465 ± 0.144	0.381 ± 0.119
(6331) 1992 FZ ₁	2.358	yes		5.321 ± 0.101	0.473 ± 0.101
(6976) Kanatsu	2.333			5.497 ± 0.116	0.307 ± 0.042
(7800) Zhongkeyuan	2.231			3.511 ± 0.157	0.389 ± 0.067
(8149) Ruff	2.323			4.091 ± 0.132	0.554 ± 0.116
(9147) Kourakuen	2.191			4.922 ± 0.080	0.241 ± 0.052
(9553) Colas	2.198			3.791 ± 0.141	0.178 ± 0.029
(10537) 1991 RY ₁₆	2.850			7.865 ± 0.269	0.313 ± 0.053
(10666) Feldberg	2.222			3.978 ± 0.038	0.233 ± 0.020
(15237) 1988 RL ₆	2.393	yes		2.557 ± 0.520	0.470 ± 0.254
(17469) 1991 BT	2.371	yes		5.999 ± 0.173	0.258 ± 0.035
(19165) Nariyuki	2.348			3.464 ± 0.196	0.487 ± 0.099
(26886) 1994 TJ ₂	2.342			2.970 ± 0.559	0.241 ± 0.163
(27343) Deannashea	2.331			2.864 ± 0.455	0.341 ± 0.113
(29796) 1999 CW ₇₇	2.344			4.851 ± 0.073	0.248 ± 0.062
(30872) 1992 EM ₁₇	2.326			3.146 ± 0.080	0.409 ± 0.050
(31414) Rotarysusa	2.260			2.822 ± 0.090	0.222 ± 0.028
(32940) 1995 UW ₄	2.189			3.351 ± 0.070	0.273 ± 0.090
(33881) 2000 JK ₆₆	2.213		yes
(38070) Redwine	2.143		

Appendix E**V-type Band Centers and Pyroxene Mineralogies**

In Table E1, we list each V-type asteroid spectrum that was analyzed, the near-infrared observation date, its temperature-corrected band centers and 1σ error, and estimated Fs (mol%) and Wo (mol%) contents derived from those band centers. Uncertainties of 0.000 for the band centers are due to small

reflectance uncertainties in the spectra, which causes the fits to derive the same band center after each spectrum is randomly resampled 99,999 times using a Gaussian distribution based on the 1σ uncertainty for each reflectance value. The Fs and Wo contents for (10537) 1991 RY₁₆ are in parentheses since its Band I center is affected by an olivine component, which would affect the calculated Fs and Wo contents.

Table E1
Band Centers and Bulk Fs and Wo contents for V-types

Asteroid	Observation Date (UT)	Temperature-corrected			
		Band Centers		Fs (mol%)	Wo (mol%)
		Band I (μm)	Band II (μm)		
(4) Vesta	2000 Oct 09	0.939 ± 0.002	1.961 ± 0.002	42.7	9.7
(4) Vesta	2001 Sep 29	0.939 ± 0.000	1.961 ± 0.001	43.1	9.9
(4) Vesta	2009 Nov 18	0.938 ± 0.001	1.971 ± 0.002	43.2	9.9
(809) Lundia	2008 Aug 12	0.953 ± 0.002	1.980 ± 0.002	52.8	13.6


Table E1
(Continued)

Asteroid	Observation Date (UT)	Temperature-corrected			
		Band Centers		Fs (mol%)	Wo (mol%)
		Band I (μm)	Band II (μm)		
(809) Lundia	2008 Aug 26	0.949 \pm 0.011	1.974 \pm 0.001	49.8	12.4
(956) Elisa	2008 Jul 05	0.943 \pm 0.000	1.981 \pm 0.001	47.4	11.5
(956) Elisa	2008 Oct 09	0.941 \pm 0.011	1.965 \pm 0.001	44.5	10.4
(1459) Magnya	2002 Mar 23	0.951 \pm 0.002	1.965 \pm 0.001	49.8	12.5
(1468) Zomba	2009 Apr 26	0.946 \pm 0.002	2.016 \pm 0.003	52.9	13.6
(1929) Kollaa	2001 Feb 19	0.951 \pm 0.002	1.956 \pm 0.002	48.8	12.1
(2011) Veteraniya	2003 Aug 14	0.939 \pm 0.002	1.965 \pm 0.005	43.5	10.0
(2011) Veteraniya	2014 Aug 26	0.943 \pm 0.000	1.962 \pm 0.000	45.0	10.6
(2045) Peking	2002 Jan 14	0.945 \pm 0.002	1.972 \pm 0.003	47.7	11.6
(2045) Peking	2003 Feb 17	0.948 \pm 0.002	1.985 \pm 0.003	50.3	12.6
(2045) Peking	2008 Aug 26	0.947 \pm 0.001	1.976 \pm 0.002	49.0	12.1
(2168) Swope	2015 Jan 16	0.950 \pm 0.000	1.933 \pm 0.000	46.1	11.0
(2168) Swope	2015 Jan 17	0.955 \pm 0.000	1.944 \pm 0.000	49.8	12.5
(2168) Swope	2015 Jan 19	0.947 \pm 0.000	1.855 \pm 0.000	35.4	6.9
(2371) Dimitrov	2009 Aug 01	0.951 \pm 0.002	1.993 \pm 0.004	53.1	13.7
(2442) Corbett	2002 Sep 15	0.945 \pm 0.002	1.952 \pm 0.003	45.4	10.8
(2511) Patterson	2004 May 07	0.945 \pm 0.002	1.968 \pm 0.002	46.7	11.3
(2566) Kirghizia	2002 May 08	0.945 \pm 0.002	1.948 \pm 0.003	44.5	10.4
(2653) Principia	2002 Nov 26	0.946 \pm 0.002	1.963 \pm 0.003	47.1	11.4
(2653) Principia	2005 Jul 16	0.942 \pm 0.000	1.975 \pm 0.002	46.2	11.0
(2763) Jeans	2004 Jun 26	0.953 \pm 0.002	1.994 \pm 0.001	54.3	14.2
(2763) Jeans	2008 Jul 05	0.949 \pm 0.000	1.978 \pm 0.001	50.5	12.7
(2763) Jeans	2008 Aug 26	0.951 \pm 0.001	2.030 \pm 0.001	57.1	15.2
(2795) Lepage	2005 Apr 09	0.942 \pm 0.002	1.958 \pm 0.002	44.4	10.4
(2851) Harbin	2001 Aug 24	0.932 \pm 0.000	1.926 \pm 0.000	34.9	6.7
(2851) Harbin	2003 Jan 12	0.936 \pm 0.002	1.930 \pm 0.002	37.6	7.8
(2912) Lapalma	2001 Feb 20	0.941 \pm 0.000	1.939 \pm 0.000	41.6	9.3
(3155) Lee	2001 Jun 22	0.928 \pm 0.002	1.913 \pm 0.002	31.5	5.4
(3155) Lee	2005 Jul 14	0.927 \pm 0.003	1.929 \pm 0.003	32.8	5.9
(3715) Štohl	2015 Jan 15	0.948 \pm 0.000	2.009 \pm 0.000	53.0	13.7
(3715) Štohl	2015 Jan 19	0.943 \pm 0.000	1.982 \pm 0.000	47.7	11.6
(3782) Celle	2002 Nov 26	0.934 \pm 0.003	1.917 \pm 0.005	35.0	6.7
(3782) Celle	2004 Jun 25	0.939 \pm 0.002	1.945 \pm 0.002	41.0	9.0
(3782) Celle	2015 Jan 15	0.936 \pm 0.000	1.933 \pm 0.000	37.8	7.8
(3782) Celle	2015 Jan 16	0.947 \pm 0.000	2.029 \pm 0.000	54.9	14.4
(3849) Incidentia	2015 Jan 16	0.954 \pm 0.000	2.009 \pm 0.000	56.9	15.2
(3849) Incidentia	2015 Jan 17	0.954 \pm 0.000	1.961 \pm 0.000	51.1	13.0
(3867) Shiretoko	2013 Jan 14	0.962 \pm 0.000	2.004 \pm 0.000	60.3	16.5
(4038) Kristina	2002 Oct 28	0.931 \pm 0.001	1.963 \pm 0.001	38.4	8.0
(4188) Kitezh	2002 Aug 14	0.946 \pm 0.000	1.957 \pm 0.002	46.4	11.2
(5111) Jacliff	2005 Sep 05	0.936 \pm 0.001	1.963 \pm 0.001	41.2	9.1
(5235) Jean-Loup	2013 Jan 14	0.941 \pm 0.000	1.948 \pm 0.000	42.4	9.6
(5560) Amytis	2013 Jan 14	0.937 \pm 0.000	1.951 \pm 0.000	40.6	8.9
(5754) 1992 FR ₂	2015 Jan 15	0.957 \pm 0.000	1.945 \pm 0.000	51.5	13.1
(5754) 1992 FR ₂	2015 Jan 19	0.937 \pm 0.000	1.955 \pm 0.000	40.8	9.0
(5875) Kuga	2014 Sep 03	0.952 \pm 0.000	1.956 \pm 0.000	49.6	12.4
(6331) 1992 FZ ₁	2013 Jan 14	0.941 \pm 0.000	1.948 \pm 0.000	42.5	9.6
(6976) Kanatsu	2013 Jan 14	0.948 \pm 0.000	1.954 \pm 0.000	46.9	11.4
(7800) Zhongkeyuan	2009 Jan 09	0.953 \pm 0.002	1.980 \pm 0.006	52.6	13.6
(8149) Ruff	2014 Sep 03	0.947 \pm 0.000	1.961 \pm 0.000	47.4	11.5
(9147) Kourakuen	2014 Aug 26	0.948 \pm 0.000	1.976 \pm 0.000	49.4	12.3
(9553) Colas	2014 Sep 03	0.939 \pm 0.000	1.917 \pm 0.000	38.2	8.0
(10537) 1991 RY ₁₆	2008 Jan 30	0.972 \pm 0.003	1.919 \pm 0.005	(56.6)	(15.2)
(10666) Feldberg	2015 Jan 16	0.944 \pm 0.000	1.977 \pm 0.000	47.5	11.6
(10666) Feldberg	2015 Jan 19	0.945 \pm 0.000	1.962 \pm 0.000	46.5	11.2
(15237) 1988 RL ₆	2014 Sep 03	0.937 \pm 0.000	1.995 \pm 0.000	45.5	10.8
(15237) 1988 RL ₆	2014 Sep 04	0.933 \pm 0.000	1.948 \pm 0.000	37.9	7.8
(17469) 1991 BT	2013 Jan 14	0.940 \pm 0.000	1.956 \pm 0.000	42.9	9.8
(19165) Nariyuki	2015 Jan 19	0.950 \pm 0.000	1.939 \pm 0.000	46.7	11.3
(26886) 1994 TJ ₂	2008 Jul 05	0.934 \pm 0.002	1.949 \pm 0.003	38.7	8.2
(27343) Deannashea	2008 Aug 26	0.937 \pm 0.002	1.939 \pm 0.002	39.1	8.3

Table E1
(Continued)

Asteroid	Observation Date (UT)	Temperature-corrected		Fs (mol%)	Wo (mol%)
		Band Centers			
		Band I (μm)	Band II (μm)		
(29796) 1999 CW ₇₇	2013 Jan 14	0.947 \pm 0.000	1.959 \pm 0.000	47.3	11.5
(30872) 1992 EM ₁₇	2013 Jan 14	0.948 \pm 0.000	1.995 \pm 0.000	51.4	13.0
(31414) Rotarysusa	2014 Sep 03	0.941 \pm 0.000	1.932 \pm 0.000	41.0	9.1
(32940) 1995 UW ₄	2014 Sep 04	0.942 \pm 0.000	2.049 \pm 0.000	54.3	14.1
(33881) 2000 JK ₆₆	2007 Nov 23	0.944 \pm 0.002	1.952 \pm 0.002	44.8	10.5
(38070) Redwine	2006 Oct 05	0.948 \pm 0.002	1.952 \pm 0.003	46.8	11.3

ORCID iDs

T. H. Burbine  <https://orcid.org/0000-0001-8889-8692>
P. C. Buchanan  <https://orcid.org/0000-0003-1648-6079>
M. J. Jercinovic  <https://orcid.org/0000-0001-5917-9509>
R. C. Greenwood  <https://orcid.org/0000-0002-5544-8027>

References

- Abdu, Y. A., Scorzelli, R. B., Souza Azevedo, I., & Varela, M. E. 2007, *M&PSA*, **42**, 5114
- Ammannito, E., De Sanctis, M. C., Capaccioni, F., et al. 2013a, *M&PS*, **48**, 2185
- Ammannito, E., De Sanctis, M. C., Palomba, E., et al. 2013b, *Natur*, **504**, 122
- Angrisani, M., Palomba, E., Longobardo, A., et al. 2023, *Icar*, **390**, 115320
- Asphaug, E. 1997, *M&PS*, **32**, 965
- Barrat, J. A., Gillet, Ph., Lesourd, M., et al. 1999, *M&PS*, **34**, 91
- Barrat, J. A., Yamaguchi, A., Greenwood, R. C., et al. 2007, *GeCoA*, **71**, 4108
- Barrat, J.-A., Yamaguchi, A., Zanda, B., et al. 2010, *GeCoA*, **74**, 6218
- Basaltic Volcanism Study Project 1981, Basaltic Volcanism on the Terrestrial Planets (New York: Pergamon), 1286
- Beck, A. W., & McSween, H. Y., Jr. 2010, *M&PS*, **45**, 850
- Beck, P., Barrat, J.-A., Grisolle, F., et al. 2011, *Icar*, **216**, 560
- Berkley, J. L., & Boynton, N. J. 1992, *Metic*, **27**, 387
- Binzel, R. P., & Xu, S. 1993, *Sci*, **260**, 186
- Birlan, M., Nedelcu, D. A., Popescu, M., et al. 2014, *MNRAS*, **437**, 176
- Buchanan, P. C. 1995, PhD thesis, Univ. Houston
- Buchanan, P. C., Lindstrom, D. J., & Mittlefehldt, D. W. 2000a, *LPICo*, **997**, 21
- Buchanan, P. C., Lindstrom, D. J., Mittlefehldt, D. W., et al. 2000b, *M&PS*, **35**, 1321
- Buchanan, P. C., & Mittlefehldt, D. W. 2003, *AMR*, **16**, 128
- Buratti, B. J., Dalba, P. A., Hicks, M. D., et al. 2013, *JGRE*, **118**, 1991
- Burbine, T. H., Buchanan, P. C., Binzel, R. P., et al. 2001, *M&PS*, **36**, 761
- Burbine, T. H., Buchanan, P. C., & Binzel, R. P. 2007, *LPSC*, **38**, 2117
- Burbine, T. H., Buchanan, P. C., Dolkar, T., & Binzel, R. P. 2009, *M&PS*, **44**, 1331
- Burbine, T. H., Buchanan, P. C., Klima, R. L., & Binzel, R. P. 2018, *JGRE*, **123**, 1791
- Burbine, T. H., Greenwood, R. C., Zhang, B., & Buchanan, P. C. 2023, *LPSC*, **54**, 2347
- Burns, R. G. 1993, *Mineralogical Applications of Crystal Field Theory* (2nd ed.; Cambridge: Cambridge Univ. Press)
- Bus, S. J. 2011, IRTF Near-IR Spectroscopy of Asteroids V2.0, EAR-A-10046-4-IRTFSPEC-V2.0. NASA Planetary Data System <https://pds.nasa.gov/ds-view/pds/viewProfile.jsp?dsid=EAR-A-10046-4-IRTFSPEC-V2.0>
- Bus, S. J., & Binzel, R. P. 2002, *Icar*, **158**, 106
- Bus, S. J., & Binzel, R. P. 2003, Small Main-belt Asteroid Spectroscopic Survey, Phase II, EAR-A-10028-4-SBN0001/SMASII-V1.0. NASA Planetary Data System <https://pds.nasa.gov/ds-view/pds/viewProfile.jsp?dsid=EAR-A-10028-4-SBN0001/SMASII-V1.0>
- Carli, C., Ciarniello, M., Migliorini, A., & Pratesi, G. 2022, *Icar*, **371**, 114653
- Cheng, H. C. J., & Klimczak, C. 2022, *JSG*, **161**, 104677
- Clenet, H., Jutzi, M., Barrat, J.-A., et al. 2014, *Natur*, **511**, 303
- Combe, J.-P., McCord, T. B., McFadden, L. A., et al. 2015, *Icar*, **259**, 53
- Davis, D. R., Durda, D. D., Marzari, F., et al. 2002, in Asteroids III, ed. W. F. Bottke et al. (Tucson, AZ: Univ. Arizona Press), 545
- De Sanctis, M. C., Ammannito, E., Capria, M. T., et al. 2012, *Sci*, **336**, 697
- De Sanctis, M. C., Ammannito, E., Capria, M. T., et al. 2013, *M&PS*, **48**, 2166
- De Sanctis, M. C., Ammannito, E., Migliorini, A., et al. 2011, *MNRAS*, **412**, 2318
- Delaney, J. S., Prinz, M., & Takeda, H. 1984, *LPSC*, **15**, C251
- Delaney, J. S., Takeda, H., Prinz, M., et al. 1983, *Metic*, **18**, 103
- Delbo, M., Gai, M., Lattanzi, M. G., et al. 2006, *Icar*, **181**, 618
- DeMeo, F. E., Binzel, R. P., Slivan, S. M., & Bus, S. J. 2009, *Icar*, **202**, 160
- Duffard, R., de León, J., Licandro, J., et al. 2006, *A&A*, **456**, 775
- Duffard, R., Lazzaro, D., Licandro, J., et al. 2004, *Icar*, **171**, 120
- Fowler, G. W., Papike, J. J., Spilde, M. N., & Shearer, C. K. 1994, *GeCoA*, **58**, 3921
- Fulvio, D., Perna, D., Ieva, S., et al. 2016, *MNRAS*, **455**, 584
- Gaffey, M. J. 1976, *JGR*, **81**, 905
- Gaffey, M. J., Cloutis, E. A., Kelley, M. S., & Reed, K. L. 2002, in Asteroids III, ed. W. F. Bottke et al. (Tucson, AZ: Univ. Arizona Press), 183
- Greenwood, R. C., Barrat, J.-A., Yamaguchi, A., et al. 2014, *E&PSL*, **390**, 165
- Grove, T. L., & Bartels, K. S. 1992, *LPSC*, **22**, 437
- Hardersen, P. S. 2016, Hardersen IRTF Asteroid NIR Reflectance Spectra V1.0, EAR-A-10046-3-HARDERSENPEC-V1.0. NASA Planetary Data System
- Hardersen, P. S., Gaffey, M. J., & Abell, P. A. 2004, *Icar*, **167**, 170
- Hardersen, P. S., Reddy, V., Cloutis, E., et al. 2018, *AJ*, **156**, 11
- Hardersen, P. S., Reddy, V., & Roberts, R. 2015, *ApJs*, **221**, 19
- Hardersen, P. S., Reddy, V., Roberts, R., & Mainzer, A. 2014, *Icar*, **242**, 269
- Harlow, G. E., Nehru, C. E., Prinz, M., et al. 1979, *E&PSL*, **43**, 173
- Harrington, R., McCoy, T., Welzenbach, L., & Sharp, Z. 2008, *AnMN*, **31**, 15
- Harris, A. W., & Lagerros, J. S. V. 2002, in Asteroids III, ed. W. F. Bottke et al. (Tucson, AZ: Univ. Arizona Press), 205
- Hewins, R. H. 1980, *LPSC*, **11**, 441
- Hicks, M. D., Buratti, B. J., Lawrence, K. J., et al. 2014, *Icar*, **235**, 60
- Hiroi, T., Binzel, R. P., Sunshine, J. M., et al. 1995, *Icar*, **115**, 374
- Hiroi, T., Pieters, C. M., & Takeda, H. 1994, *M&PS*, **29**, 394
- Ieva, S., Dotto, E., Lazzaro, D., et al. 2016, *MNRAS*, **455**, 2871
- Jenkins, M. C., Mungall, J. E., Zientek, M. L., et al. 2021, *PreR*, **367**, 106457
- Jutzi, M., Asphaug, E., Gillet, P., et al. 2013, *Natur*, **494**, 207
- Kelley, M. S., Vilas, F., Gaffey, M. J., & Abell, P. A. 2003, *Icar*, **165**, 215
- Kojima, H., & Yamaguchi, A. 2005, *Meteorite Newsletter*, **13**, 18
- Larson, H. P., & Fink, U. 1975, *Icar*, **26**, 420
- Lazzaro, D., Michtchenko, T., Carvano, J. M., et al. 2000, *Sci*, **288**, 2033
- Leith, T. B., Moskovitz, N. A., Mayne, R. G., et al. 2017, *Icar*, **295**, 61
- Li, J.-Y., Le Corre, L., Schröder, S. E., et al. 2013, *Icar*, **226**, 1252
- Lim, L. F., Emery, J. P., & Moskovitz, N. A. 2011, *Icar*, **213**, 510
- Macke, R. J., Britt, D. T., & Consolmagno, G. J. 2011, *M&PS*, **46**, 311
- Mainzer, A. K., Bauer, J. M., Cutri, R., et al. 2016, NEOWISE Diameters and Albedos V1.0, EAR-A-COMPIL-5-NEOWISEDIAM-V1.0. NASA Planetary Data System <https://pds.nasa.gov/ds-view/pds/viewDataset.jsp?dsid=EAR-A-COMPIL-5-NEOWISEDIAM-V1.0>
- Marlow, R., & Mason, B. 1990, *AnMN*, **13**, 20
- Mason, B. 1981, *AnMN*, **4**, 46
- Mayne, R. G., McSween, H. Y., Jr., McCoy, T. J., & Gale, A. 2009, *GeCoA*, **73**, 794
- Mayne, R. G., Sunshine, J. M., McSween, H. Y., Jr., et al. 2011, *Icar*, **214**, 147
- McBride, K., Corrigan, C., & McCoy, T. 2005, *AnMN*, **28**, 22

- McBride, K., & McCoy, T. 2000, *AnMN*, 23, 19
- McBride, K., & McCoy, T. 2003, *AnMN*, 26, 23
- McBride, K., McCoy, T., & Welzenbach, L. 2001a, *AnMN*, 24, 13
- McBride, K., McCoy, T., & Welzenbach, L. 2001b, *AnMN*, 24, 20
- McBride, K., McCoy, T., & Welzenbach, L. 2003a, *AnMN*, 26, 18
- McBride, K., McCoy, T., & Welzenbach, L. 2003b, *AnMN*, 26, 19
- McBride, K., McCoy, T., & Welzenbach, L. 2004, *AnMN*, 27, 19
- McCord, T. B., Adams, J. B., & Johnson, T. V. 1970, *Sci*, **168**, 1445
- McSween, H. Y., Ammannito, E., Reddy, V., et al. 2013a, *JGRE*, **118**, 335
- McSween, H. Y., Mittlefehldt, D. W., Beck, A. W., et al. 2012, in *The Dawn Mission to Minor Planets 4 Vesta and 1 Ceres*, ed. C. Russell & C. Raymond (New York: Springer), 141
- McSween, H. Y., Jr., Binzel, R. P., De Sanctis, M. C., et al. 2013b, *M&PS*, **48**, 2090
- McSween, H. Y., Jr., Raymond, C. A., Stolper, E. M., et al. 2019, *ChEG*, **79**, 125526
- Meteoritical Bulletin Database 2023, <https://www.lpi.usra.edu/meteor/>
- Michel, P., Benz, W., & Richardson, D. C. 2003, *Natur*, **421**, 608
- Michel, P., Benz, W., & Richardson, D. C. 2004, *Icar*, **168**, 420
- Michtchenko, T. A., Lazzaro, D., Ferraz-Mello, S., & Roig, F. 2002, *Icar*, **158**, 343
- Migliorini, A., De Sanctis, M. C., Lazzaro, D., & Ammannito, E. 2017, *MNRAS*, **464**, 1718
- Migliorini, A., De Sanctis, M. C., Michtchenko, T. A., et al. 2021, *MNRAS*, **504**, 2019
- Mitchell, J. T., Tomkins, A. G., Newton, C., & Johnson, T. E. 2021, *E&PSL*, **571**, 117105
- Mittlefehldt, D. W. 2005, *M&PS*, **40**, 665
- Mittlefehldt, D. W. 2015, *ChEG*, **75**, 155
- Mittlefehldt, D. W., Greenwood, R. C., Berger, E. L., et al. 2022, *M&PS*, **57**, 484
- Mittlefehldt, D. W., Herrin, J. S., Quinn, J. E., et al. 2013, *M&PS*, **48**, 2105
- Mittlefehldt, D. W., & Lindstrom, M. M. 1997, *GeCoA*, **61**, 453
- Mittlefehldt, D. W., McCoy, T. J., Goodrich, C. A., & Kracher, A. 1998, in *Planetary Materials*, ed. J. J. Papike (Berlin: De Gruyter), 4
- Moskovitz, N. A., Jedicke, R., Gaidos, E., et al. 2008a, *Icar*, **198**, 77
- Moskovitz, N. A., Lawrence, S., Jedicke, R., et al. 2008b, *ApJ*, **682**, L57
- Moskovitz, N. A., Willman, M., Burbine, T. H., et al. 2010, *Icar*, **208**, 773
- Ostrowski, D., & Bryson, K. 2019, *P&SS*, **165**, 148
- Papike, J. J. 1980, in *Pyroxenes*, ed. C. T. Prewitt (Berlin: De Gruyter), 495
- Prettyman, T. H., Mittlefehldt, D. W., Yamashita, N., et al. 2012, *Sci*, **338**, 242
- Rayner, J. T., Toomey, D. W., Onaka, P. M., et al. 2003, *PASP*, **115**, 362
- Reddy, V., & Sanchez, J. A. 2016, *Reddy Main Belt Asteroid Spectra V1.0*, *EAR-A-10046-3-REDDYMBSPEC-V1.0*. NASA Planetary Data System <https://pds.nasa.gov/ds-view/pds/viewDataset.jsp?dsid=EAR-A-10046-3-REDDYMBSPEC-V1.0>
- Reddy, V., Sanchez, J. A., Nathues, A., et al. 2012, *Icar*, **217**, 153
- Righter, K. 2022, *AnMN*, 45, 2
- Righter, K., & Drake, M. J. 1997, *M&PS*, **32**, 929
- Roush, T. L., & Singer, R. B. 1986, *JGR*, **91**, 10301
- Russell, C. T., Raymond, C. A., Coradini, A., et al. 2012, *Sci*, **336**, 684
- Satterwhite, C., & Mason, B. 1989, *AnMN*, 12, 14
- Satterwhite, C., & Mason, B. 1992, *AnMN*, 15, 30
- Satterwhite, C., & Mason, B. 1993a, *AnMN*, 16, 18
- Satterwhite, C., & Mason, B. 1993b, *AnMN*, 16, 19
- Schenk, P., O'Brien, D. P., Marchi, S., et al. 2012, *Sci*, **336**, 694
- Schenk, P. M., Neesemann, A., Marchi, S., et al. 2022, *M&PS*, **57**, 22
- Schwarz, C., Mason, B., McCoy, T., & Lindstrom, D. 1996, *AnMN*, 19, 13
- Score, R., & Mason, B. 1983, *AnMN*, 6, 1
- Score, R., & Mason, B. 1986a, *AnMN*, 9, 16
- Score, R., & Mason, B. 1986b, *AnMN*, 9, 18
- Score, R., & Mason, B. 1988a, *AnMN*, 11, 16
- Score, R., & Mason, B. 1988b, *AnMN*, 11, 20
- Score, R., & Mason, B. 1996, *AnMN*, 19, 12
- Score, R., & Reid, A. 1980, *AnMN*, 3, 5
- Scott, E. R. D., Greenwood, R. C., Franchi, I. A., & Sanders, I. S. 2009, *GeCoA*, **73**, 5835
- Shearer, C. K., Burger, P., & Papike, J. J. 2010, *GeCoA*, **74**, 4865
- 2023, *SMASS* <http://smass.mit.edu/catalog.php>
- Steele, I. M., & Smith, J. V. 1976, *E&PSL*, **33**, 67
- Stolper, E. 1977, *GeCoA*, **41**, 587
- Sykes, M. V., & Vilas, F. 2001, *EP&S*, **53**, 1077
- Takeda, H. 1997, *M&PS*, **32**, 841
- Takeda, H., Mori, H., & Yanai, K. 1981, *PolRe*, **20**, 81
- Tedesco, E. F., Noah, P. V., Noah, M., & Price, S. D. 2004, *IRAS Minor Planet Survey*, *IRAS-A-FPA-3-RDR-IMPS-V6.0*. NASA Planetary Data System <https://pds.nasa.gov/ds-view/pds/viewProfile.jsp?dsid=IRAS-A-FPA-3-RDR-IMPS-V6.0>
- Thomas, P. C., Binzel, R. P., Gaffey, M. J., et al. 1997, *Sci*, **277**, 1492
- Treiman, A. H. 1997, *M&PS*, **32**, 217
- Vaci, Z., Day, J. M. D., Paquet, M., et al. 2021, *NatCo*, **12**, 5443
- Warren, P. H., & Jerde, E. A. 1987, *GeCoA*, **51**, 713
- Wiechert, U. H., Halliday, A. N., Palme, H., & Rumble, D. 2004, *E&PSL*, **221**, 373
- Wilson, L., & Keil, K. 1996, *JGR*, **101**, 18927
- Wittmann, A., Hiroi, T., Ross, D. K., et al. 2011, *LPSC*, **42**, 1984
- Xu, S., Binzel, R. P., Burbine, T. H., & Bus, S. J. 1995, *Icar*, **115**, 1
- Yamaguchi, A., Barrat, J.-A., Ito, M., & Bohn, M. 2011, *JGRE*, **116**, E08009
- Yamaguchi, A., Clayton, R. N., Mayeda, T. K., et al. 2002, *Sci*, **296**, 334
- Yamaguchi, A., Mori, H., & Takeda, H. 1993, *Metic*, **28**, 462
- Zema, M., Domeneghetti, M. C., Molin, G. M., & Tazzoli, V. 1997, *M&PS*, **32**, 855
- Zema, M., Domeneghetti, M. C., & Tazzoli, V. 1999, *AmMin*, **84**, 1895
- Zolensky, M. E., Weisberg, M. K., Buchanan, P. C., & Mittlefehldt, D. W. 1996, *M&PS*, **31**, 518